

Trajectory Optimization for DDE Models of Supercavitating Underwater Vehicles

Carlo L. Bottasso* and Francesco Scorcelletti

*Dipartimento di Ingegneria Aerospaziale,
Politecnico di Milano, Via La Masa 34, Milano 20156, Italy*

Massimo Ruzzene and Seong S. Ahn

*School of Aerospace Engineering, Georgia Institute of Technology,
270 Ferst Dr., Atlanta, GA 30332-0150, USA*

Abstract

We focus on solving trajectory optimization problems for supercavitating underwater vehicles. These vehicles are characterized by a substantially reduced hydrodynamic drag with respect to fully wetted systems, being in contact with water only at the nose where a cavitator generates a cavity that completely envelops the body, at the fins which pierce the cavity and are used to control the system, and on the vehicle after-body. This unique loading configuration, the complex and non-linear interactions between vehicle and cavity, and memory effects associated with the advection of disturbances downstream from the cavitator make the problem of modeling and maneuvering of supercavitating vehicles particularly challenging.

In this study we first develop a flight mechanics model for supercavitating vehicles which is formulated to account for the dependence of the cavity shape from the past history of the system. This mathematical model is governed by a particular class of Delay Differential Equations, featuring time delays on the states of the system. Flight trajectories and maneuvering strategies for supercavitating vehicles are here obtained through the solution of an optimal control problem, whose solution, given a cost function and general constraints and bounds on states and controls, yields the control time histories that maneuver the vehicle according to a desired strategy, together with the associated flight path. The optimal control problem is solved using a novel direct multiple shooting approach, which is formulated to properly handle conditions dictated by the Delay Differential Equations formulation governing the dynamic behavior of the vehicle. Specifically, the new formulation enforces the state continuity line conditions in a least-squares sense using local interpolations, which supports local time stepping and drastically reduces the number of optimization unknowns.

Examples of maneuvers and resulting trajectories demonstrate the effectiveness of the proposed methodology and the generality of the formulation. Results are also compared with those obtained from a previously developed model governed by Ordinary Differential Equations to highlight differences and demonstrate the need for the current formulation.

Keywords: supercavitating vehicles, flight mechanics, trajectory optimization, maneuvers, optimal control.

*Electronic address: carlo.bottasso@polimi.it

I. INTRODUCTION

When a body moves through water at sufficient speed, the fluid pressure drops locally below the level that sustains the liquid phase, and a low-density gaseous cavity forms. Flows exhibiting cavities entirely enveloping the moving body are termed *supercavitating* flows. In supercavitating flows, the liquid phase does not contact the moving body over most of its length, thus making the skin friction drag almost negligible. Several new and projected supercavitating underwater vehicles exploit supercavitation as a means to achieve extremely high submerged speeds and low drag [1]. The size of existing or notional supercavitating high-speed bodies ranges from that of projectiles to heavy-weight full-scale torpedoes.

Recent research efforts have led to important advances in the comprehension, modeling and simulation of supercavitating vehicles. The development of reliable and effective theoretical and computational procedures is particularly important for the future design of such vehicles. For example, a variety of computational methods for supercavitating flows, including Boundary Element Methods (BEM) and first-principle simulation procedures based on state-of-the-art computational fluid dynamics, have been used for the prediction of cavity shape, drag, as well as body-cavity and fin-water-cavity interactional forces [2]. In parallel to these efforts, flight mechanics simulators have been developed to assess the flight dynamics characteristics of this class of vehicles, and for the development and the analysis of proper control strategies [3–5].

The control and maneuvering of supercavitating vehicles presents unique challenges associated with their distinctive operating conditions, which are affected by the location of the hydrodynamic force generated by the cavitator with respect to the center of gravity, the complex and non-linear nature of the interactional forces between vehicle and cavity, the dynamic nature of the cavity itself, the need for roll control during curved flight [3], as well as the presence of hull vibrations induced by after-body planing, surfing and tail-slapping [6].

To support the study and understanding of these complex phenomena and the design of such vehicles, in this paper we present a novel formulation of the trajectory optimization problem for supercavitators. The paper extends previous investigations by the authors [7], by introducing a refined, more accurate cavity model which accounts for time delay effects related to the cavity formation process, and their influence on the hydrodynamic vehicle/body interactions. The resulting flight mechanics model is governed by a set of Delay Differential

Equations (DDEs), as opposed to the Ordinary Differential Equations (ODEs) which are obtained when the delay effects are neglected [7]. The optimal control problem defining extremal trajectories and controls is solved numerically through a novel numerical approach based on a Direct Multiple Shooting (DMS) technique.

The term trajectory optimization refers to the process of computing the optimal control inputs and the ensuing response of a mathematical model of a vehicle, which minimize a cost function (or maximize an index of performance) while satisfying given constraints (which specify, for example, the vehicle flight envelope boundaries). Notice that this problem differs significantly from the usual and more common problem of forward simulation starting from given initial conditions under the action of control inputs. In general, in order to use a vehicle flight simulator, one has to specify the control inputs applied to the vehicle, or a trajectory or sequence of trim conditions that the vehicle flight control system should track. In a trajectory optimization problem none of these two pieces of information, controls or trajectory, are known, so that standard forward simulators can not be used directly.

In fact, whenever one wants to verify the vehicle performance in unsteady maneuvering flight at the boundaries of the flight envelope, the use of a standard forward simulator poses important difficulties, since one has to hypothesize the necessary control inputs to fly that maneuver or the vehicle trajectory, both being unknown. Since this process is particularly difficult when the vehicle operates close to its flight envelope boundaries, one is in fact unable to determine with precision and confidence which is the maximum theoretical performance of the vehicle, and this inevitably leads to conservative design or restrictions on its operation.

To answer these needs, trajectory optimization codes implement appropriate numerical methods which, interacting with forward simulators, augment their capabilities in order to compute the controls which fly the vehicle model in an optimal and constraint-satisfying way. Software procedures for automatically and reliably solving trajectory optimization problems represent valuable tools in the design and development of a new vehicle. Given the high complexity of the flight mechanics characteristics of supercavitating vehicles, we believe that trajectory optimization procedures have a high potential for significantly improving the design process, as recently explored in Ref. [8].

The paper is organized in 5 sections. This introduction is followed by a detailed description of the flight mechanics model of the vehicle presented in Section II, while Section III describes the formulation of the trajectory optimization as an optimal control problem, and

its numerical solution through the proposed technique. Section IV presents a series of examples, which demonstrate the capabilities of the proposed approach, highlight differences with the previous model and illustrate some of the characteristics of the dynamic behavior of the considered class of vehicles. Finally, Section V summarizes the main results of the work and outlines future research directions.

II. FLIGHT MECHANICS MODEL

A. Vehicle Configuration and Controls

A six degrees-of-freedom rigid body model describes the dynamic behavior of the vehicle, whose basic configuration is depicted in Fig. 1. The vehicle is controlled by a one-degree-of-freedom cavitator, by four fins arranged according to a cruciform configuration, and by the propulsion thrust. Additional forces acting on the vehicle include gravity and possible interactions with the cavity. It is assumed that the two horizontal fins are mechanically interconnected and have a common rotation axis, while the two vertical fins can be controlled independently.

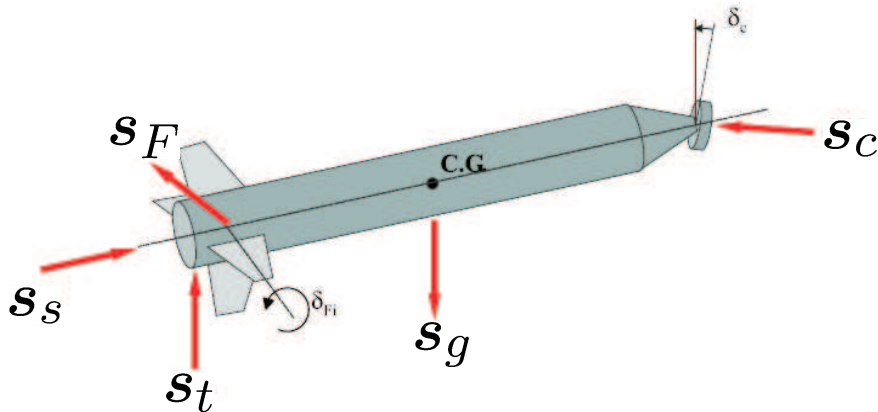


FIG. 1: Schematic of the vehicle configuration.

B. Equations of Motion

The vehicle equations of motion are conveniently written with respect to a body-attached frame denoted by $\mathcal{F}_{P,\mathcal{B}}$ with origin in P and triad $\mathcal{B} = (\mathbf{b}_1, \mathbf{b}_2, \mathbf{b}_3)$. An inertial reference frame

$\mathcal{F}_{O,\mathcal{I}}$ is centered at the point O and has a triad of unit vectors $\mathcal{I} = (\mathbf{i}_1, \mathbf{i}_2, \mathbf{i}_3)$ as shown in Fig. 2. The equations of balance of linear and angular momentum (Euler's equations) in the body-attached frame can be written as:

$$\dot{\mathbf{l}}^{\mathcal{B}} + \boldsymbol{\omega}^{\mathcal{B}} \times \mathbf{l}^{\mathcal{B}} = \mathbf{s}^{\mathcal{B}}, \quad (1a)$$

$$\dot{\mathbf{h}}_P^{\mathcal{B}} + \mathbf{v}_P^{\mathcal{B}} \times \mathbf{l}^{\mathcal{B}} + \boldsymbol{\omega}^{\mathcal{B}} \times \mathbf{h}_P^{\mathcal{B}} = \mathbf{m}_P^{\mathcal{B}}, \quad (1b)$$

where the linear momentum is $\mathbf{l} = m\mathbf{v}_P + \mathbf{S}_P^T \boldsymbol{\omega}$, and the angular momentum is given by $\mathbf{h}_P = \mathbf{S}_P \mathbf{v}_P + \mathbf{J}_P \boldsymbol{\omega}$. Denoting with ρ_V the vehicle density, $m = \int_V \rho_V dV$ is the total mass of the system, $\mathbf{S}_P = \int_V \rho_V \mathbf{r} \times dV$ is the first moment of inertia and $\mathbf{J}_P = - \int_V \rho_V \mathbf{r} \times \mathbf{r} \times dV$ is the inertia dyadic. The linear velocity of the point P is denoted by \mathbf{v}_P , while $\boldsymbol{\omega}$ is the angular velocity of the body frame with respect to the inertial frame; \mathbf{s} e \mathbf{m}_P are the resultants of the applied forces and moments, respectively. Here and in the following, the notation $(\cdot)^{\mathcal{A}}$ denotes the components in the generic \mathcal{A} triad. If \mathbf{R} is the rotation tensor that brings triad \mathcal{I} into triad \mathcal{B} , then components of a generic vector \mathbf{a} in the two triads are related as $\mathbf{a}^{\mathcal{I}} = \mathbf{R} \mathbf{a}^{\mathcal{B}}$. Furthermore \mathbf{a}_{\times} is the skew-symmetric tensor associated with \mathbf{a} . Finally, the symbol $(\dot{\cdot}) = d \cdot / dt$ indicates a derivative with respect to time.

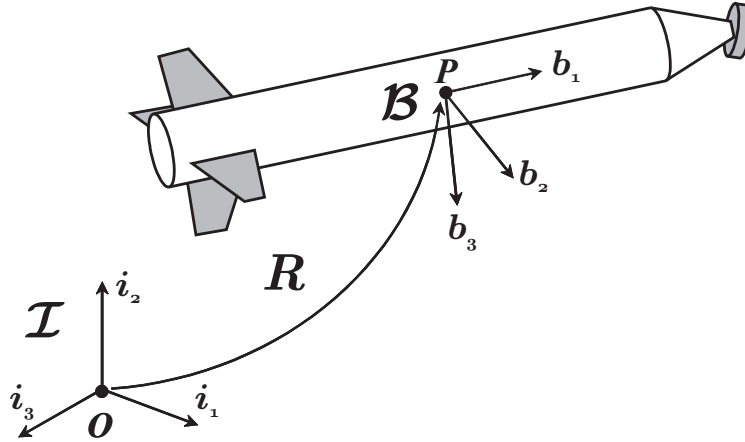


FIG. 2: Inertial and body frames.

Equations (1) can be rewritten in the following compact form:

$$\mathbf{M}^{\mathcal{B}} \dot{\mathbf{w}}^{\mathcal{B}} + \mathbf{w}^{\mathcal{B}} \times \mathbf{M}^{\mathcal{B}} \mathbf{w}^{\mathcal{B}} = \mathbf{f}^{\mathcal{B}}, \quad (2)$$

where the generalized inertia tensor is defined as:

$$\mathbf{M} = \begin{bmatrix} m\mathbf{I} & \mathbf{S}_P^T \\ \mathbf{S}_P & \mathbf{J}_P \end{bmatrix}, \quad (3)$$

and where the generalized velocity \mathbf{w} and the generalized force \mathbf{f} are respectively defined as:

$$\mathbf{w} = (\mathbf{v}_P^T, \boldsymbol{\omega}^T)^T, \quad \mathbf{f} = (\mathbf{s}^T, \mathbf{m}_P^T)^T. \quad (4)$$

In the compact dynamics equation (2), the symbol $(\cdot)_{\times}$ denotes the South-West product [9]:

$$\mathbf{w}_{\times} = \begin{bmatrix} \boldsymbol{\omega}_{\times} & \mathbf{0} \\ \mathbf{v}_{P_{\times}} & \boldsymbol{\omega}_{\times} \end{bmatrix}. \quad (5)$$

The position and orientation of the vehicle are respectively expressed through a position vector $\mathbf{r}_P = (P - O)$ and a set of rotation parameters collected in the vector \mathbf{e} , quaternions in this work. The kinematics relations are expressed as:

$$\dot{\mathbf{d}} = \begin{bmatrix} \mathbf{R}(\mathbf{e}) & \mathbf{0} \\ \mathbf{0} & \mathbf{E}(\mathbf{e}) \end{bmatrix} \mathbf{w}^B, \quad (6)$$

where \mathbf{d} is the vector of generalized coordinates defined as:

$$\mathbf{d} = (\mathbf{r}_P^{IT}, \mathbf{e}^T)^T, \quad (7)$$

The total force acting on the vehicle is the sum of several terms, which can be written:

$$\mathbf{s} = \mathbf{s}_g + \mathbf{s}_s + \mathbf{s}_c + \sum_{i=1}^4 \mathbf{s}_{F_i} + \mathbf{s}_t, \quad (8)$$

where \mathbf{s}_g is the gravity force, \mathbf{s}_s the thrust, \mathbf{s}_c the force on the cavitator, \mathbf{s}_{F_i} the resultant on the i th fin, \mathbf{s}_t the contact force due to the interaction between the vehicle and the cavity.

The total moment \mathbf{m}_P can be computed as:

$$\mathbf{m}_P = \mathbf{r}_{GP} \times \mathbf{s}_g + \mathbf{r}_{SP} \times \mathbf{s}_s + \mathbf{r}_{CP} \times \mathbf{s}_c + \sum_{i=1}^4 \mathbf{r}_{F_i P} \times \mathbf{s}_{F_i} + \mathbf{r}_{TP} \times \mathbf{s}_t + \mathbf{m}_t. \quad (9)$$

\mathbf{r}_{GP} denotes the position vector of the center of gravity from the point P ; similarly \mathbf{r}_{SP} and \mathbf{r}_{CP} identify the points of application of the propulsion thrust and the cavitator force, respectively. The current model neglects hydrodynamic moments on cavitator and on the fins.

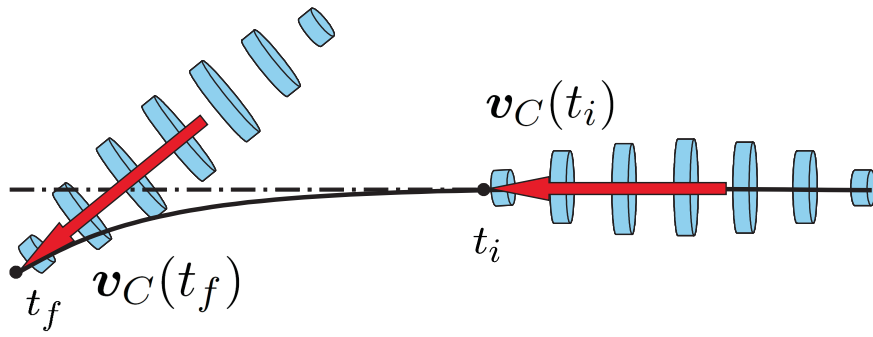
C. Cavity Model

The behavior of the cavity affects the forces at the nose of the vehicle, the immersion of the fins in the fluid, and the contact forces between vehicle and cavity boundary. More

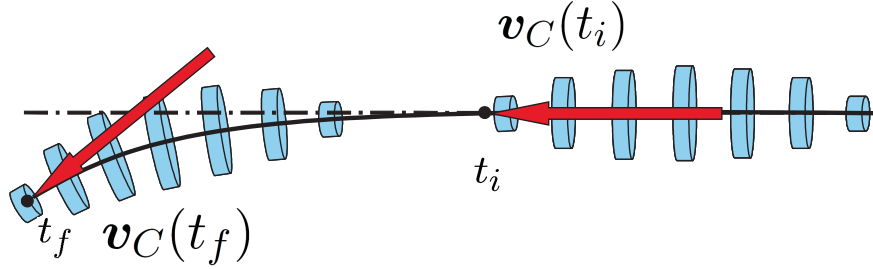
specifically, planing and fin forces strongly depend on the dynamic behavior of the vehicle and on the hydrodynamic characteristics of the cavity. The vehicle velocity affects the cavity shape and size, which in turn modify the extension of the immersed area of the vehicle and the magnitude of the resulting planing and fin forces. As a result, the vehicle-cavity system is highly coupled. This work considers a cavity model based on Logvinovich’s formulation [10]. In this regard, the present formulation extends previously published work by the authors [7], where all cavity dynamics phenomena were neglected. The previous formulation was based on the assumption that the cavity shape is instantaneously defined by the velocity of the nose at the considered instant of time. In that case, the cavity axis is defined by the straight line aligned with the nose velocity vector, and the shape and size are defined by the speed of the nose, among other parameters. This obviously crude approximation results however in a very convenient formulation for the flight mechanics model, which is governed by a set of ODEs, and for the associated trajectory optimization problem.

Logvinovich’s model is based on the principle that each cavity section expands independently from adjacent ones. The expansion of each section is determined by the state of motion of the cavitator when the cavity is generated. As a result, perturbations of the cavitator state of motion produce cavity distortions which propagate towards the after-body according to the vehicle history of motion, and influence hydrodynamic cavity/vehicle interactions with a certain time lag. This delay, known in the literature as “memory effect”, has important consequences on the vehicle dynamic behavior and needs to be properly accounted for in simulations, during the design and optimization of control strategies for maneuvering flight, and the analysis of stability. The differences in cavity shape predicted according to the two models are illustrated in Fig. 3. This schematic representation assumes that the vehicle is performing a turn according to the trajectory represented by the solid line. Snapshots of the cavity configuration at two instants of time show that, in the absence of memory effects, the cavity is aligned with the velocity of the nose (Fig. 3.(a)), while when memory effects are included, it tends to develop around the trajectory of the nose (Fig. 3.(b)). This different behavior, highly amplified in the figure for demonstration purposes, carries important implications with respect to the estimation of the hydrodynamic forces on the fins and on the vehicle after-body.

The cavity model considered in this work therefore assumes that the cavity axis is defined by the past trajectory of the cavitator. Referring to Fig. 4, the cavitator trajectory at the



(a) Cavity configuration without memory effects.



(b) Cavity configuration with memory effects.

FIG. 3: Schematic of cavity configurations predicted through different cavity models and with the inclusion of time delay.

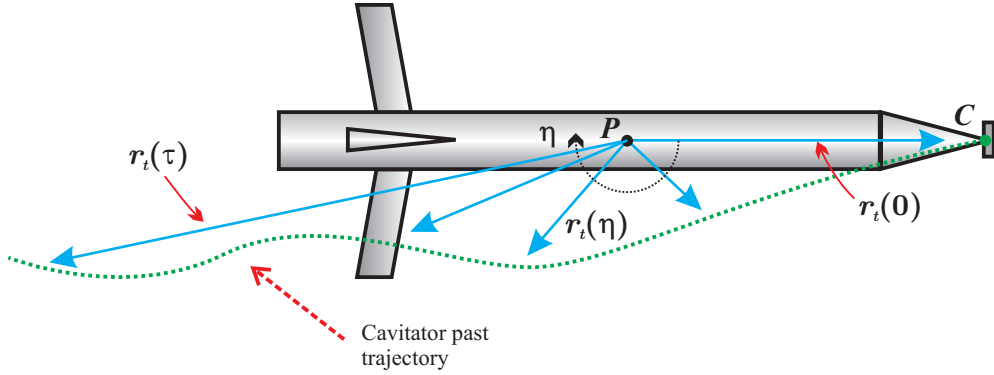


FIG. 4: Cavity model.

generic time instant t can be described in terms of a vector with origin at point $P(t)$, expressed as a function of a delay variable η :

$$\mathbf{r}_t(\eta), \quad \eta \in [0, \tau]. \quad (10)$$

By taking $\tau = t$ one describes the whole trajectory traced by the cavitator during the entire flight; in practice this is not necessary, since we will be simply interested in finding the

interactions of fins and after-body with the cavity, so that τ can be chosen such that point $\mathbf{r}_t(\tau)$ is just passed the vehicle after-body, since the shape of the cavity axis passed that point is irrelevant for the evaluation of the current state of motion.

The inertial components of the cavity axis trajectory are readily computed on the knowledge of the past history of the reference point vector inertial components $\mathbf{r}_P^{\mathcal{I}}$ and of the orientation parameters \mathbf{e} , which should therefore be stored during the integration process. In fact, we have

$$\mathbf{r}_t^{\mathcal{I}}(\eta) = \mathbf{r}_C^{\mathcal{I}}(t - \eta) - \mathbf{r}_P^{\mathcal{I}}(t), \quad (11)$$

where the past locations of the cavitator, $\mathbf{r}_C^{\mathcal{I}}(t - \eta)$, are computed in terms of the past locations of the reference point P on the vehicle as

$$\mathbf{r}_C^{\mathcal{I}}(t - \eta) = \mathbf{r}_P^{\mathcal{I}}(t - \eta) + \mathbf{r}_{CP}^{\mathcal{I}}(t - \eta), \quad (12)$$

and

$$\mathbf{r}_{CP}^{\mathcal{I}}(t - \eta) = \mathbf{R}^T(\mathbf{e}(t - \eta)) \mathbf{r}_{CP}^{\mathcal{B}}, \quad (13)$$

where $\mathbf{r}_{CP}^{\mathcal{B}} = \text{const.}$

Once the function expressed by Eq. (11) is known, the curve tangent vector is calculated as:

$$\boldsymbol{\tau}(\eta) = \frac{d\mathbf{r}_t(\eta)}{d\eta}, \quad (14)$$

while the curve length parameter originating from the cavitator is

$$\xi(\eta) = \int_0^\eta \left| \frac{d\mathbf{r}_t(\hat{\eta})}{d\hat{\eta}} \right| d\hat{\eta}. \quad (15)$$

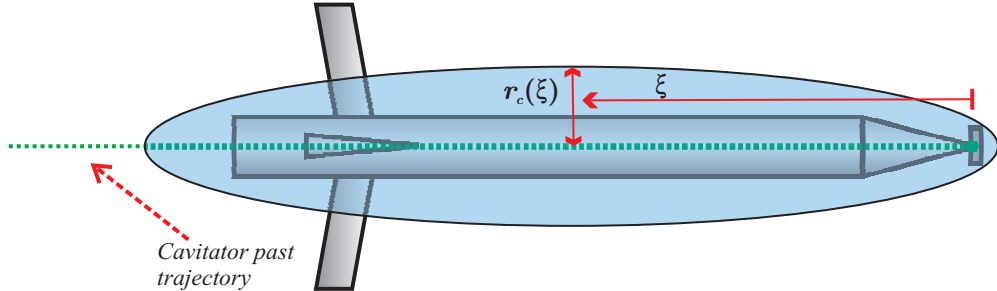


FIG. 5: Cavity model.

According to Logvinovich's model [10], the local cavity radius is defined in terms of the curve length parameter ξ :

$$r_c(\xi) = \frac{d_{\max}}{2} \sqrt{1 - (1 - k_1^2)|1 - k_2(\xi)|^{1/0.85}}, \quad (16)$$

where the maximum cavity diameter d_{\max} is given by

$$d_{\max} = d_c \sqrt{0.82 \frac{1 + \sigma}{\sigma}}, \quad (17)$$

while the variables k_1 e $k_2(\xi)$ are defined as

$$k_1 = 1.92 \left(0.82 \frac{1 + \sigma}{\sigma} \right)^{-1/2}, \quad (18a)$$

$$k_2 = \frac{\xi - d_c}{l_m}, \quad (18b)$$

In Eq. (18b), l_m denotes a reference length to be computed as follows:

$$l_m = \frac{d_{\max}}{2} \left(\frac{1.92}{\sigma} - 3 \right), \quad (19)$$

where σ is the cavitation number defined as

$$\sigma = \frac{(p_\infty - p_c)}{\frac{1}{2} \rho_w v_C^2}, \quad (20)$$

with

$$p_\infty = \rho_w g h + p_{\text{atm}},$$

where p_∞ and p_c are the ambient fluid pressure and a reference cavity vapor pressure, respectively. Also, v_C , ρ_w , g , h , and p_{atm} are respectively the speed of the cavitator, the fluid (water) density, gravity acceleration, the underwater depth, and the atmospheric pressure on the water surface.

Finally, the rate of radial expansion for the cavity is given by the following expression:

$$\dot{r}_c(\xi) = \frac{r_{\max}^2}{0.85 r_c} \frac{2 v_C}{l_m} (1 - k_1^2)^{1/0.85} |1 - k_2(\xi)|^{3/8.5}. \quad (21)$$

D. Vehicle Force Models

The generalized force vector is the sum of several terms:

$$\mathbf{f} = \mathbf{f}_g + \mathbf{f}_s + \mathbf{f}_c + \sum_{i=1}^4 \mathbf{f}_{F_i} + \mathbf{f}_t. \quad (22)$$

\mathbf{f}_g denotes the contribution of the gravity force, \mathbf{f}_s is the contribution of the propulsion thrust, \mathbf{f}_c is the generalized force acting on the cavitator, \mathbf{f}_{F_i} the force term associated with

the i th fin, finally \mathbf{f}_t the generalized interaction force. The gravity force depends only on the vehicle orientation so that we can write:

$$\mathbf{f}_g^{\mathcal{B}}(t) = \mathbf{f}_g^{\mathcal{B}}(\mathbf{e}(t)). \quad (23)$$

The propulsion thrust is supposed to be aligned to the longitudinal axis of the vehicle and its magnitude is defined by the throttle value $\delta_s \in [0, 1]$ and by the maximum available thrust T_{\max} :

$$\mathbf{f}_s^{\mathcal{B}}(t) = (T_{\max}\delta_s(t), 0, 0, 0, 0, 0)^T. \quad (24)$$

The remaining generalized forces \mathbf{f}_c , \mathbf{f}_{F_i} , \mathbf{f}_t , are of hydrodynamic nature and are described in detail in the following sections.

1. Cavitator Force Model

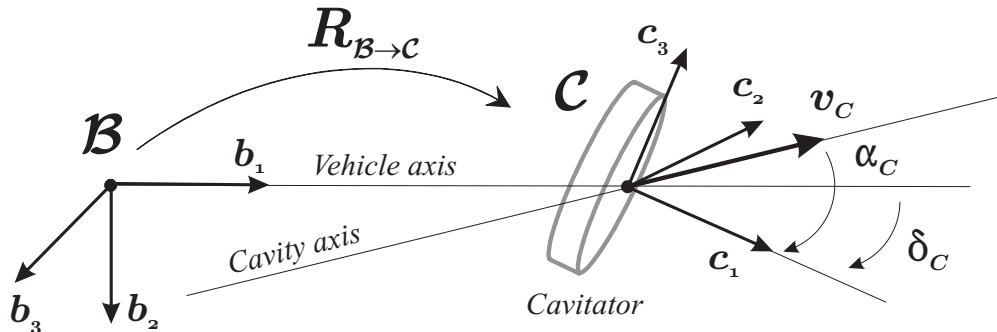


FIG. 6: Body frame and cavitator frame.

The main purpose of the cavitator is to generate a supercavity, and to act as a control surface. The configuration of Fig. 1 assumes that the cavitator disk rotation axis is parallel to the elevator axis, with a pitch-up cavitator rotation considered as positive. The hydrodynamic forces acting on the cavitator can be conveniently expressed in terms of a reference frame $\mathcal{F}_{C,C}$ with origin at the cavitator center C and with triad $\mathcal{C} = (\mathbf{c}_1, \mathbf{c}_2, \mathbf{c}_3)$ shown in Fig. 6. The unit vector \mathbf{c}_1 is perpendicular to the disk surface and its orientation with respect to the vehicle axis \mathbf{b}_1 is defined by the control angle δ_c , so that the components of \mathbf{c}_1 in the body-fixed triad \mathcal{B} are

$$\mathbf{c}_1^{\mathcal{B}} = (\cos \delta_c, 0, \sin \delta_c)^T. \quad (25)$$

The unit vector \mathbf{c}_2 is orthogonal to the plane defined by vectors \mathbf{v}_C and \mathbf{c}_1 :

$$\mathbf{c}_2 = \frac{\mathbf{v}_C \times \mathbf{c}_1}{|\mathbf{v}_C \times \mathbf{c}_1|}, \quad (26)$$

where \mathbf{v}_C is the cavitator velocity. Finally, \mathbf{c}_3 completes a right handed triad such that $\mathbf{c}_3 = \mathbf{c}_1 \times \mathbf{c}_2$. Given the cavitator triad \mathcal{C} , the velocity of the cavitator $\mathbf{v}_C^{\mathcal{C}}$ has components

$$\mathbf{v}_C^{\mathcal{C}} = (u_C^{\mathcal{C}}, 0, w_C^{\mathcal{C}})^T, \quad (27)$$

which define the cavitator angle of attack as the angle between vectors \mathbf{v}_C and \mathbf{c}_1 :

$$\tan \alpha_C = \frac{w_C^{\mathcal{C}}}{u_C^{\mathcal{C}}}. \quad (28)$$

The force acting on the cavitator belongs to the plane identified by the two vectors \mathbf{v}_C and \mathbf{c}_1 , and can be decomposed into lift and drag components, which are given by [11]

$$L_C = \frac{1}{2} \rho_w v_C^2 A_C C_D(\sigma, 0) \sin \alpha_C \cos \alpha_C, \quad (29a)$$

$$D_C = \frac{1}{2} \rho_w v_C^2 A_C C_D(\sigma, 0) \cos^2 \alpha_C, \quad (29b)$$

where A_C is the disk area, while $C_D(\sigma, 0)$ is the drag coefficient at zero angle of attack and cavitation number σ , which is given by [12] $C_D(\sigma, 0) = C_{D0}(1 + \sigma)$.

The generalized force on the cavitator can be expressed in the body-fixed triad through a change of components to assume the general form

$$\mathbf{f}_c^{\mathcal{B}}(t) = \mathbf{f}_c^{\mathcal{B}}(\mathbf{w}^{\mathcal{B}}(t), \delta_c(t)), \quad (30)$$

which highlights the dependency upon the body-attached generalized velocity components $\mathbf{w}^{\mathcal{B}}$ of the vehicle and upon the control angle δ_c .

2. Fin Force Model

Fins are symmetric surfaces with zero sweepback and cuneiform section, assumed constant along the span. The forces acting on the generic fin are described according to the conventions shown in Figs. 7 and 8.

It is convenient to introduce two local reference frames: the first is defined by the triad $\hat{\mathcal{F}}_i = (\hat{\mathbf{f}}_1, \hat{\mathbf{f}}_2, \hat{\mathbf{f}}_3)$ and identifies the undeflected fin configuration, while the second $\mathcal{F}_i = (\mathbf{f}_1, \mathbf{f}_2, \mathbf{f}_3)$ follows the fin in its deflected configuration. Both frames have origin at the

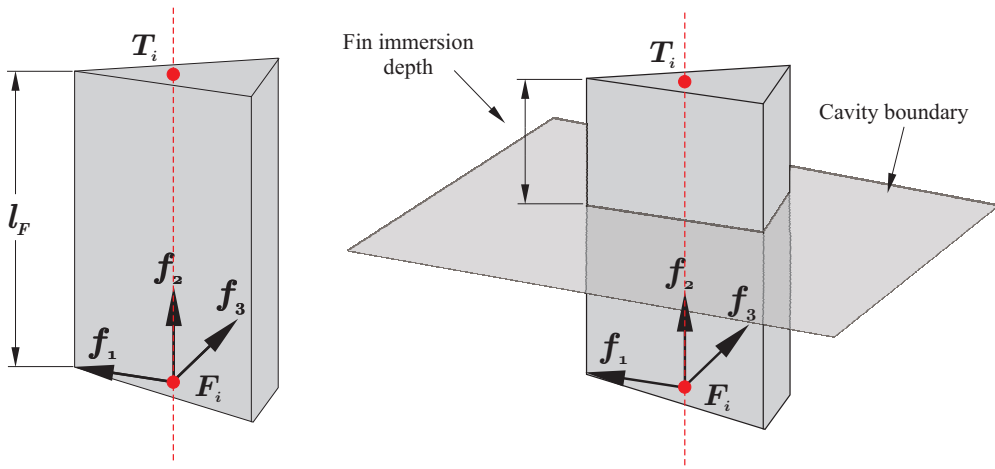


FIG. 7: 3D view of a fin.

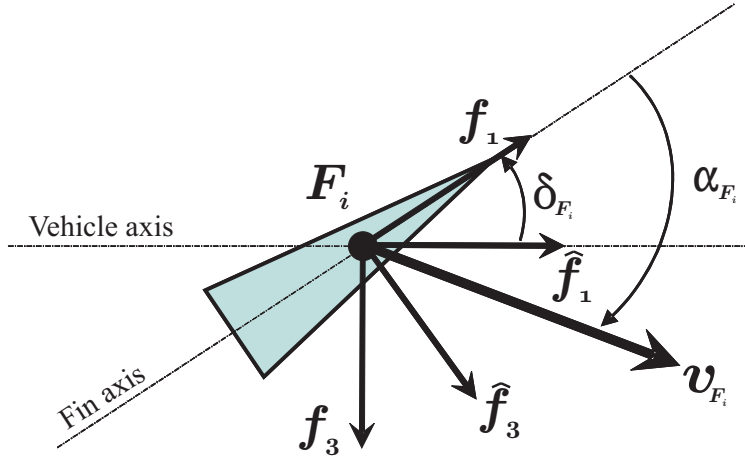


FIG. 8: Fin frames.

point F_i which is located at the intersection between the fin rotation axis and root. The frame $\hat{\mathcal{F}}_i$ is defined by $\hat{\mathbf{f}}_1 = \mathbf{b}_1$, and

$$\hat{\mathbf{f}}_2 = \mathbf{b}_1 \times \mathbf{n}, \quad (31)$$

where

$$\mathbf{n} = \frac{\mathbf{r}_{F_i P} \times \mathbf{r}_{T_i P}}{|\mathbf{r}_{F_i P} \times \mathbf{r}_{T_i P}|}, \quad (32)$$

with $\mathbf{r}_{F_i P}$ and $\mathbf{r}_{T_i P}$ respectively denoting the position vectors of the tip and the root of the generic fin from the reference point P .

The fin axis is identified by the following unit vector:

$$\mathbf{a}_i = \frac{\mathbf{r}_{T_i P} - \mathbf{r}_{F_i P}}{|\mathbf{r}_{T_i P} - \mathbf{r}_{F_i P}|}. \quad (33)$$

Finally, the third unit vector of the triad is found as $\hat{\mathbf{f}}_3 = \hat{\mathbf{f}}_1 \times \hat{\mathbf{f}}_2$. The fin attached triad \mathcal{F}_i is obtained by rotating the reference frame $\hat{\mathcal{F}}_i$ of $\delta_{F_i} \hat{\mathbf{f}}_2$, where δ_{F_i} is the fin deflection control angle. Accordingly, the rotation tensor that brings $\hat{\mathcal{F}}_i$ onto \mathcal{F}_i is

$$\mathbf{R}_{\hat{\mathcal{F}}_i \rightarrow \mathcal{F}_i} = \begin{bmatrix} +\cos \delta_{F_i} & 0 & +\sin \delta_{F_i} \\ 0 & 1 & 0 \\ -\sin \delta_{F_i} & 0 & +\cos \delta_{F_i} \end{bmatrix}. \quad (34)$$

The resultant force on the generic fin is given by

$$\mathbf{s}_{F_i}^{\mathcal{F}_i} = \frac{1}{2} \rho_l v_{F_i}^2 S \mathbf{C}_f(\alpha_{F_i}, d_{F_i}), \quad (35)$$

where S is the fin area, v_{F_i} is the fin speed, and $\mathbf{C}_f(\alpha_{F_i}, d_{F_i})$ is a vector of force hydrodynamic coefficients. The components of \mathbf{C}_f depend on the angle of attack α_{F_i} and on the wetted span percentage $d_{F_i} \in [0, 1]$. Figure 9 shows the variation of the components of the force coefficients with respect to angle of attack for several relative immersions, obtained through BEM numerical simulations reported in Ref. [13]. The slope change corresponding to $\alpha_{F_i} \simeq 2$ deg is associated with the discontinuous transition between the two flow regimes of partial cavitation and supercavitation.

The fin velocity can be computed as

$$\mathbf{v}_{F_i} = \mathbf{v}_P + \boldsymbol{\omega} \times \mathbf{r}_{F_i^*P}, \quad (36)$$

where F_i^* denotes the point along the fin axis located at the center of the wetted portion, whose position is given by

$$\mathbf{r}_{F_i^*P} = \mathbf{r}_{F_iP} + \left(1 - \frac{d_{F_i}}{2}\right) l_F \mathbf{a}_i, \quad (37)$$

where l_F denotes the fin length. Introducing the following notation

$$\mathbf{v}_{F_i}^{\mathcal{F}_i} = (u_{F_i}^{\mathcal{F}_i}, v_{F_i}^{\mathcal{F}_i}, w_{F_i}^{\mathcal{F}_i})^T, \quad (38)$$

the fin angle of attack is defined as

$$\tan \alpha_{F_i} = \frac{w_{F_i}^{\mathcal{F}_i}}{u_{F_i}^{\mathcal{F}_i}}. \quad (39)$$

In order to explain the procedure used to evaluate the relative immersion d_{F_i} , we refer to Fig. 10. We denote with H_i the point along the fin axis where the fin pierces the cavity. The position vector of H_i from the reference point P is computed as

$$\mathbf{r}_{H_iP}(d_{F_i}) = \mathbf{r}_{F_iP} + (1 - d_{F_i}) l_F \mathbf{a}_i. \quad (40)$$

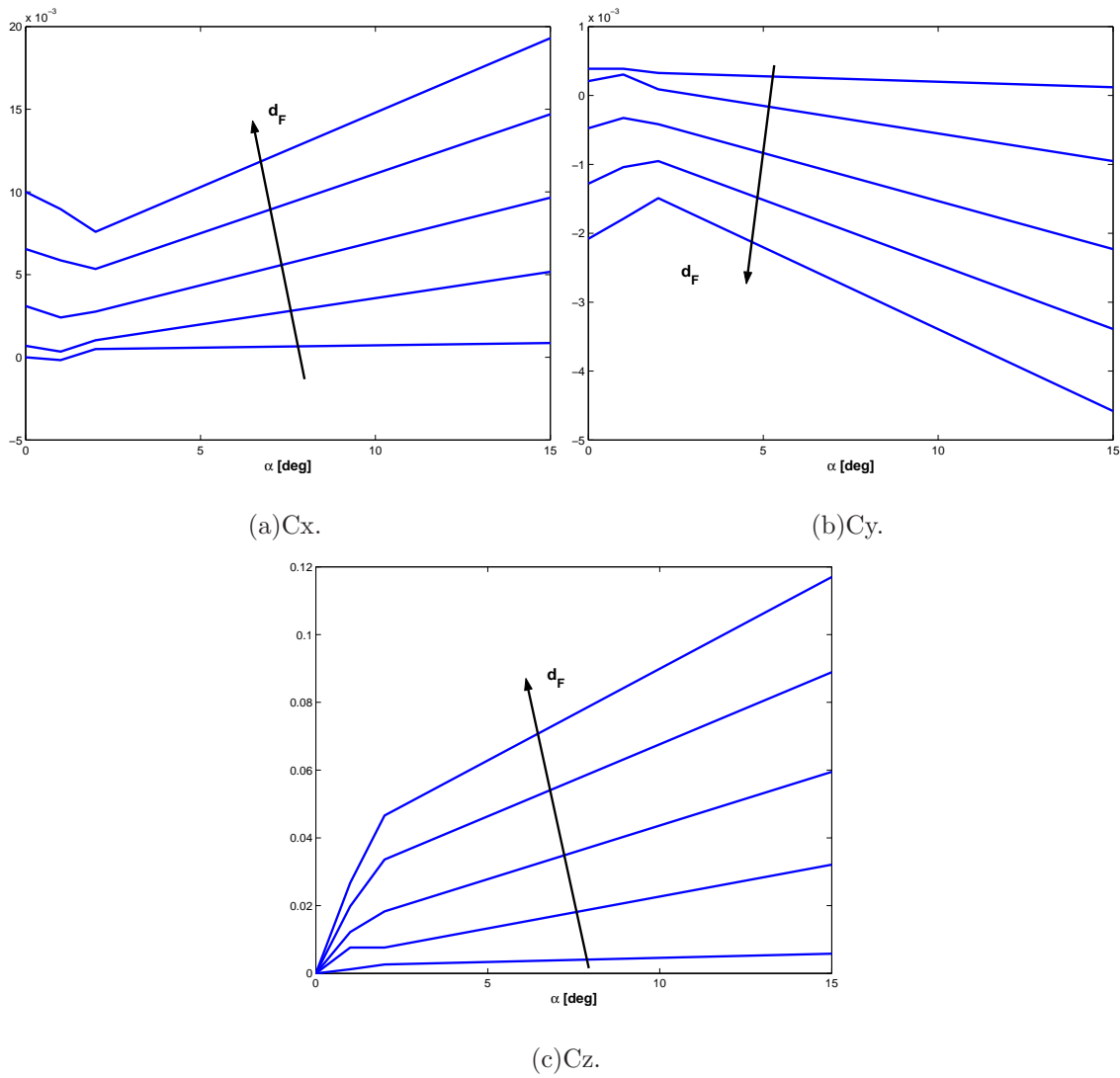


FIG. 9: Force coefficients with respect to angle of attack for several relative immersions ($d_F = \{0.1, 0.3, 0.5, 0.7, 0.9\}$).

The distance between H_i and the generic point belonging to the cavity axis can be written as

$$d_i(d_{F_i}, \eta) = |\mathbf{r}_{H_i P}(d_{F_i}) - \mathbf{r}_t(\eta)|. \quad (41)$$

The fin penetration depth is defined by the minimum distance between the cavity axis and point H_i . Such distance corresponds to the local cavity radius, which in turn is defined by the formation process based on the motion of the cavitator at the instant when the corresponding cavity section begins to form. Also, the temporal abscissa η_i is associated with the evolution of the cavity section at this particular point. Both relative immersion d_{F_i} and temporal abscissa η_i can be computed by solving the following non-linear system of

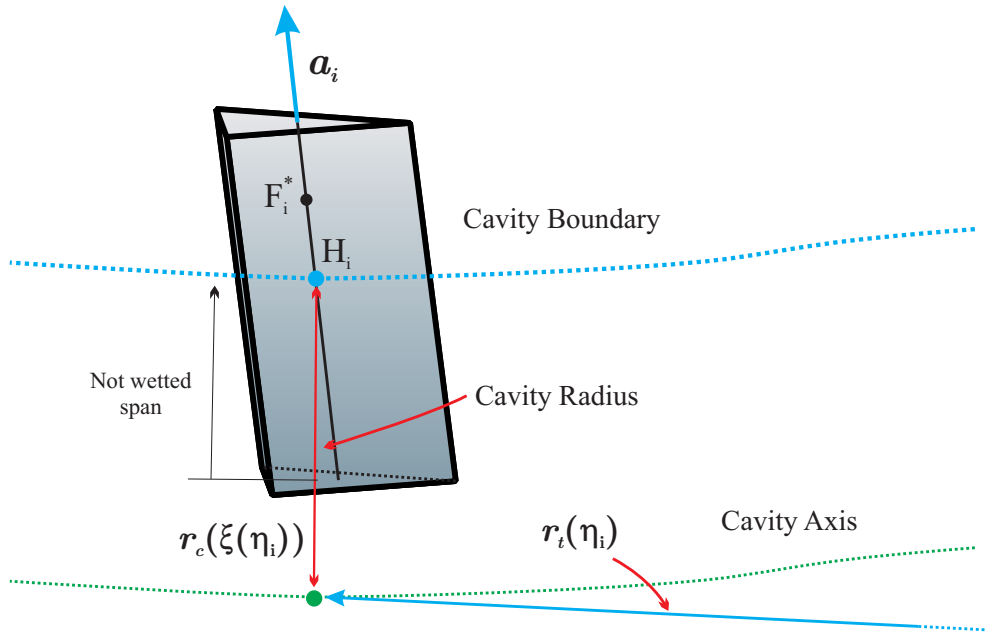


FIG. 10: Fin immersion evaluation.

equations:

$$\frac{\partial (d_i(d_{F_i}, \eta_i))^2}{\partial \eta} = 0, \quad (42a)$$

$$d_i(d_{F_i}, \eta_i) - r_c(\xi(\eta_i)) = 0, \quad (42b)$$

which upon manipulation can be expressed as

$$\boldsymbol{\tau}(\eta_i) \cdot (\mathbf{r}_{H_i P}(d_{F_i}) - \mathbf{r}_t(\eta_i)) = 0, \quad (43a)$$

$$d_i(d_{F_i}, \eta_i) - r_c(\xi(\eta_i)) = 0. \quad (43b)$$

Based on this formulation, the generalized force acting on the i th fin can be written as

$$\mathbf{f}_{F_i}^{\mathcal{B}}(t) = \mathbf{f}_{F_i}^{\mathcal{B}}(\mathbf{e}(t), \mathbf{w}^{\mathcal{B}}(t), \delta_{F_i}(t), \mathbf{r}_P^{\mathcal{I}}(t - \eta_i), \mathbf{e}(t - \eta_i), \mathbf{w}^{\mathcal{B}}(t - \eta_i)), \quad \eta_i \in [0, \tau], \quad (44)$$

which highlights the dependence of the force components on the fin control angle δ_{F_i} , on the body-attached generalized velocity components of the vehicle $\mathbf{w}^{\mathcal{B}}$, and on the vehicle orientation \mathbf{e} . In addition, the force depends on the cavity radius and orientation, which essentially are defined by the position, orientation and generalized velocity of the vehicle at the inception of the cavity formation. Such a dependency on the past history of the system and the associated delay η_i play an important role in defining the flight mechanics characteristics of the vehicle.

3. Vehicle/Cavity Interactions

The vehicle/cavity interactions are based on Hassan's model [14], which provides expressions for the force and moment acting on a cylindrical body planing over a flat or cylindrical fluid surface. Hassan's approach can be applied under the assumption of small penetration of the body into the fluid and it is based on Logvinovich's work on the two-dimensional impact of a planar shape into a non-viscous fluid [10, 15].

Referring to Fig. 11, we define a local reference frame $\mathcal{F}_{T,\mathcal{T}}$, with origin at the center T of the tail section of the vehicle, and with triad $\mathcal{T} = (\mathbf{t}_1, \mathbf{t}_2, \mathbf{t}_3)$

$$\mathbf{t}_1 = \mathbf{b}_1, \quad (45a)$$

$$\mathbf{t}_2 = \mathbf{b}_1 \times \boldsymbol{\tau}_t, \quad (45b)$$

$$\mathbf{t}_3 = \mathbf{t}_1 \times \mathbf{t}_2. \quad (45c)$$

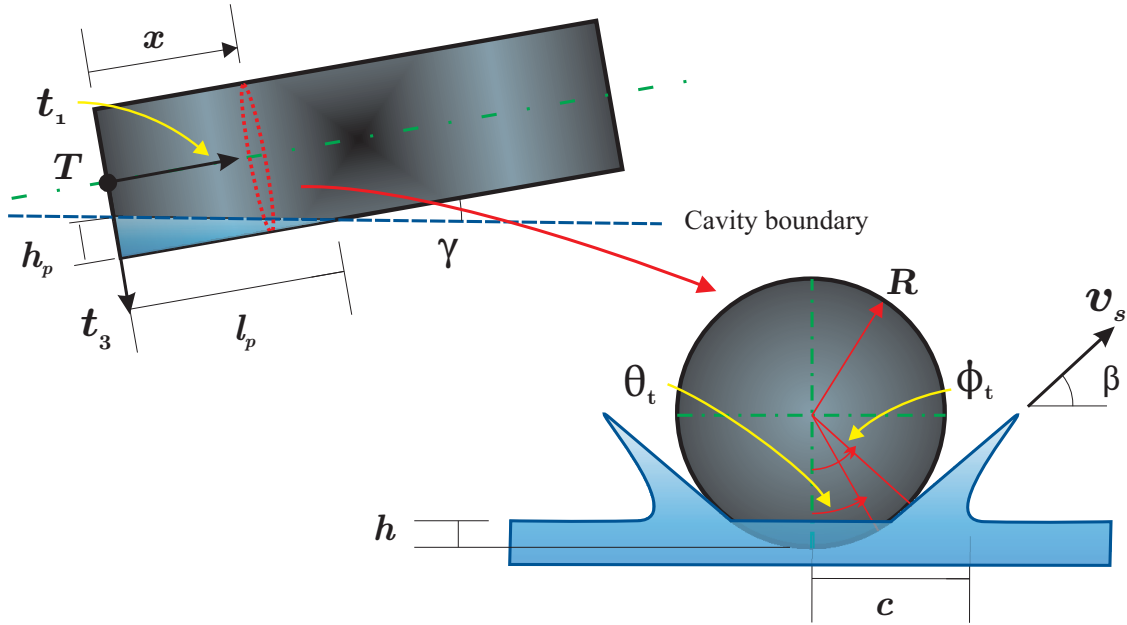


FIG. 11: Schematic of Vehicle/Cavity interaction.

The symbol $\boldsymbol{\tau}_T$ denotes the unit vector locally tangent to the cavity axis. Using Eq. (14), $\boldsymbol{\tau}_T$ can be computed as follows:

$$\boldsymbol{\tau}_T = \frac{\boldsymbol{\tau}(\eta_T)}{|\boldsymbol{\tau}(\eta_T)|}. \quad (46)$$

where η_T denotes the temporal variable corresponding to the time of formation of the cavity section at the tail location T . The value of η_T is obtained through a procedure similar to

the one followed for the calculation of the immersion of the fins. The distance between a generic point along the cavitator past trajectory and point T is expressed as

$$d_T(\eta) = |\mathbf{r}_{TP} - \mathbf{r}_t(\eta)|. \quad (47)$$

The variable η_T can be computed by solving the following non-linear equation

$$\frac{d(d_T(\eta_T))^2}{d\eta} = 0, \quad (48)$$

rewritten as

$$\boldsymbol{\tau}(\eta_T) \cdot (\mathbf{r}_t(\eta_T) - \mathbf{r}_{TP}) = 0. \quad (49)$$

Based on Hassan's model [14], the interaction between a cylindrical body and a cylindrical fluid surface can be expressed as

$$\mathbf{s}_p = \pi \rho_l (r_c(\xi_T))^2 v_e^2 \sin \alpha_e \cos \alpha_e \left(\frac{R + h_p}{R + 2h_p} \right) \left(1 - \left(\frac{\Delta}{\Delta + h_p} \right)^2 \right) (-\mathbf{t}_3), \quad (50a)$$

$$\mathbf{m}_p = \pi \rho_l (r_c(\xi_T))^2 v_e^2 \cos \alpha_e^2 \left(\frac{R + h_p}{R + 2h_p} \right) \left(\frac{h_p^2}{\Delta + h_p} \right) (+\mathbf{t}_2), \quad (50b)$$

where R is the cylinder radius and h_p is the maximum immersion depth of the body. Variable Δ has the following definition

$$\Delta = R - r_c(\xi_T), \quad (51)$$

with $r_c(\xi_T)$ denoting the local cavity radius, while $\xi_T = \xi(\eta_T)$ is the corresponding curve length associated with the cavity section expansion delay η_T (see Eq. (15)). Also in Eq. (50), α_e and v_e , respectively, are the effective angle of attack and the effective speed of the vehicle tail. The latter can be computed by projecting the velocity of point T on the $\mathbf{t}_1 - \mathbf{t}_3$ plane and augmenting this projection with the local cavity expansion rate. Given the tail velocity $\mathbf{v}_T = \mathbf{v}_P + \boldsymbol{\omega} \times \mathbf{r}_{TP}$, the relative velocity between vehicle and cavity can be obtained as

$$\mathbf{v}_r = \mathbf{v}_T - \dot{r}_c \mathbf{r}, \quad (52)$$

where \dot{r}_c is the cavity expansion rate given by Eq. (21), while \mathbf{r} is a radial unit vector computed as

$$\mathbf{r} = \mathbf{t}_2 \times \boldsymbol{\tau}_T. \quad (53)$$

Introducing the following notation

$$\mathbf{v}_r^{\mathcal{I}} = (u_r^{\mathcal{I}}, v_r^{\mathcal{I}}, w_r^{\mathcal{I}})^T, \quad (54)$$

the effective velocity v_e is

$$v_e = \sqrt{(u_r^T)^2 + (w_r^T)^2}, \quad (55)$$

while the effective angle of attack is defined by the following relation:

$$\tan \alpha_e = \frac{w_r^T}{u_r^T}. \quad (56)$$

Hassan's theory includes also a viscous effect model. In particular the fluid friction generates the following force and moment:

$$\mathbf{s}_f = \frac{1}{2} \rho_l v_e^2 \cos \alpha_e^2 C_d S_w (-\mathbf{t}_1), \quad (57a)$$

$$\mathbf{m}_f = \frac{1}{2} \rho_l v_e^2 \cos \alpha_e^2 C_d S_{wm} (-\mathbf{t}_2). \quad (57b)$$

The drag coefficient can be computed by considering the results used for turbulent flows over a smooth flat foil [16], which gives

$$C_d = \frac{0.031}{Re^{1/7}}, \quad (58)$$

where Re is the Reynolds number. Referring to the notation of Fig. 11, the wetted area S_w and wetted area including moment arm S_{wm} are respectively defined as

$$S_w = \int_0^{l_p} 2R \phi_t(x) dx, \quad (59a)$$

$$S_{wm} = \int_0^{l_p} \int_0^{\phi_t(x)} 2R^2 \cos \theta_t d\theta_t dx = \int_0^{l_p} 2R^2 \sin \phi_t(x) dx. \quad (59b)$$

Finally, the total cavity vehicle interaction force \mathbf{s}_t and moment \mathbf{m}_{t_T} about point T can be computed as

$$\mathbf{s}_t = \mathbf{s}_p + \mathbf{s}_f, \quad (60a)$$

$$\mathbf{m}_{t_T} = \mathbf{m}_p + \mathbf{m}_f. \quad (60b)$$

Transporting the moment to point P and stacking force and moment vectors, one obtains even in this case the expression of the generalized force vector. Therefore, similarly to the fin force contribution, also the vehicle/cavity interaction model depends on past vehicle position, past vehicle orientation and past generalized velocity, i.e.:

$$\mathbf{f}_t^B(t) = \mathbf{f}_t^B(\mathbf{e}(t), \mathbf{w}^B(t), \mathbf{r}_P^T(t - \eta_T), \mathbf{e}(t - \eta_T), \mathbf{w}^B(t - \eta_T)), \quad \eta_T \in [0, \tau]. \quad (61)$$

III. TRAJECTORY OPTIMIZATION

A. Overview

In this work we are interested in computing maneuvers of supercavitating vehicles. In the context of this paper, computing a maneuver means determining the time histories of the vehicle controls and the associated time histories of vehicle states which satisfy a certain number of requirements, as detailed in the following. First, maneuvers must be compatible with the vehicle dynamics, i.e. they must satisfy the equations of motion within the admissible limits imposed by the vehicle flight envelope and the necessarily limited control authority of the vehicle actuators. Clearly, this requirement is also relevant to the guidance and navigation problem. In fact, guiding a supercavitating vehicle along a compatible maneuver becomes a much simpler task than when trajectories are specified upfront, for example through spline interpolation of given way-points. Such strategies may in fact easily result in unfeasible trajectories, especially when aggressive and high performance maneuvering is required. Second, maneuvers should possibly be optimal in some sense, i.e. they should minimize some cost function, such as the time necessary to accomplish a given goal, or maximize the final vehicle velocity, or yet again the control effort necessary to steer the vehicle. In fact, optimality provides a way to select one meaningful solution among the typically infinite possible different ways of achieving a same goal. Finally, maneuvers must satisfy possible operational constraints imposed by the vehicle user in order to satisfy safety, cost, effectiveness and other needs.

B. Delay Differential Equations

The supercavitating vehicle model described in the previous section, can be more synthetically described by the following system of DDEs:

$$\dot{\mathbf{y}}(t) = \mathbf{z}(\mathbf{y}(t), \mathbf{y}(t - \eta_1), \dots, \mathbf{y}(t - \eta_M), \mathbf{u}(t)), \quad (62)$$

where $\mathbf{y} \in \mathbb{R}^{n_y}$ and $\mathbf{u} \in \mathbb{R}^{n_u}$ denote respectively state and control vectors, and $\mathbf{z} : \mathbb{R}^{n_y} \times \mathbb{R}^{M \cdot n_y} \times \mathbb{R}^{n_u} \longrightarrow \mathbb{R}^{n_y}$. The time delays are defined in Eq. (62) by M time variables η_1, \dots, η_M , which, at each time instant are evaluated by solving a set of non-linear algebraic equations:

$$\mathbf{g}(\mathbf{y}(t - \eta_1), \dots, \mathbf{y}(t - \eta_M)) = 0, \quad (63)$$

where $\mathbf{g} : \mathbb{R}^{Mn_y} \rightarrow \mathbb{R}^M$. As previously detailed, these delay-defining equations express kinematic conditions which yield the points where each fin pierces the cavity, and the point of interaction between cavity and after-body. When integrating Eq. (62) over a certain time interval Ω , it is convenient to define the upper bound for the maximum delay as:

$$\tau = \max_{t \in \Omega} \{\eta_1, \dots, \eta_M\}. \quad (64)$$

The forward simulation process in the presence of time delays on the states is slightly different with respect to the ODE case. In particular, the assigned initial conditions need to provide information on the states over a time interval prior to the initial integration time instant. The duration of such interval is quantified by the maximum delay τ defined above. The integration of Eq. (62) over the time interval $\Omega = [T_0, T]$, requires assigning the following time functions

$$\mathbf{u}(t) = \bar{\mathbf{u}}(t), \quad t \in \Omega, \quad (65a)$$

$$\mathbf{y}(T_0 - \eta) = \mathbf{y}_0(\eta), \quad \eta \in [0, \tau], \quad (65b)$$

where $\bar{\mathbf{u}}(t)$ is the assigned control time history, while $\mathbf{y}_0(\eta)$ is a time function defining a line initial condition. Notice that in the ODE case, in contrast to the DDE one, only the definition of a point initial condition at time $t = T_0$ is required.

C. Maneuver Optimal Control Problem with Time Delay

We consider the problem of determining the extremal states $\mathbf{y}_{\text{opt}}(t)$ and controls $\mathbf{u}_{\text{opt}}(t)$ which minimize an assigned cost function over the time domain $\Omega = [T_0, T] \subset \mathbb{R}$, according to a given set of constraints. We consider a cost function expressed as

$$J = \phi^b(\mathbf{y}, \mathbf{u}, t)|_{\Gamma} + \int_{\Omega} L(\mathbf{y}, \mathbf{u}, t) dt, \quad (66)$$

where the first term defines a boundary cost, with $\Gamma = \{T_0, T\}$ denoting the boundary of the domain Ω , while the second is the integral term of the cost function. The optimal solution must satisfy the dynamic compatibility conditions

$$\dot{\mathbf{y}}(t) - \mathbf{z}(\mathbf{y}(t), \mathbf{y}(t - \eta_1), \dots, \mathbf{y}(t - \eta_M), \mathbf{u}(t)) = 0, \quad (67a)$$

$$\mathbf{g}(\mathbf{y}(t - \eta_1), \dots, \mathbf{y}(t - \eta_M)) = 0, \quad (67b)$$

initial and final line conditions

$$\mathbf{y}(T_0 - \eta) \in [\mathbf{y}_{\min}^0(\eta), \mathbf{y}_{\max}^0(\eta)], \quad (68a)$$

$$\mathbf{y}(T - \eta) \in [\mathbf{y}_{\min}^T(\eta), \mathbf{y}_{\max}^T(\eta)], \quad (68b)$$

with $\eta \in [0, \tau]$, non-linear constraints involving states and controls

$$\mathbf{z}(\mathbf{y}, \mathbf{u}, t) \in [\mathbf{z}_{\min}, \mathbf{z}_{\max}], \quad (69)$$

integral conditions

$$\int_{\Omega} \mathbf{h}(\mathbf{y}, \mathbf{u}, t) dt \in [\mathbf{h}_{\min}, \mathbf{h}_{\max}], \quad (70)$$

and lower and upper bounds for states and controls

$$\mathbf{y}(t) \in [\mathbf{y}_{\min}, \mathbf{y}_{\max}], \quad (71a)$$

$$\mathbf{u}(t) \in [\mathbf{u}_{\min}, \mathbf{u}_{\max}]. \quad (71b)$$

D. Numerical Solution by Multiple Shooting

The classical approach used for the solution of optimal control problems is based on the idea of defining an augmented cost function obtained by adjoining the model governing equations (67) and all other constraints (68a)–(71b) to the performance index (66) through the use of Lagrange multipliers (co-states). Next, the stationary of the augmented index is imposed [17]; this yields the optimal control governing equations, which can then be discretized and solved numerically with an appropriate algorithm. This approach, termed the indirect method, is however not always convenient [18], especially when the model governing equations are highly complex as in the present case. Furthermore, the presence of time delays in the equations would render the derivation of the optimal control governing equations for such a complex vehicle model a daunting task. In contrast, direct methods are based on the idea of first discretizing the model governing equations on the temporal domain. Next, the problem cost function, boundary conditions and constraints are expressed in terms of the discrete parameters associated with the adopted discretization. This process defines a finite-dimensional Non-Linear Programming (NLP) problem, which is finally solved numerically. Therefore, instead of first optimizing and then discretizing as in the indirect method, with the direct method one first discretizes and then optimizes, quite often a much simpler and viable

approach for very complex system models. The presence of time delays in the equations does not pose insurmountable additional difficulties, as will be shown here below.

There are two main approaches to the discretization of the direct problem, namely the Direct Transcription (DT) and the Direct Multiple Shooting (DMS) techniques [18]. Both techniques reduce the original problem to a discrete parameter optimization. However, for DMS the accuracy in the solution of the system dynamics response does not drive the dimension of the associated NLP problem, while the opposite is true for DT. In other words, with the DMS technique, the choice of the integration time step, which ultimately is dictated by the integration algorithm and by the solution time scales which need to be accurately resolved for the problem at hand, does not affect the number of optimization parameters. This is in marked contrast with the DT approach.

In this work, we consider typical delays τ which may be significantly smaller than the simulation time span $\Delta T = T - T_0$. For accuracy, the discretization time step h must be significantly smaller than the typical delay τ :

$$h \ll \tau, \tag{72}$$

and, accordingly

$$\Delta T \gg \tau \gg h. \tag{73}$$

This potentially leads to a very large number of integration/discretization steps. This fact motivates the selection of DMS as the direct method to be used in the current study. In fact, the use of DT with such large numbers of time steps would lead to extremely large NLP problems, and hence to high computational costs.

In summary, in the present work we solve the maneuver optimal control problems of supercavitating vehicles using a novel Direct Multiple Shooting technique for Delay Differential Equations (DMSDDE), which is described fully in Ref. [19], and which is reviewed in the following.

We consider a partition of the time domain Ω given by $0 = t_0 < t_1 < \dots < t_{N_a} = T$ with $\Omega^i = [t_i, t_{i+1}]$, $i = 0, \dots, N_a - 1$, where each Ω^i is a shooting segment. Here and in the following, quantities associated with the generic vertex between segments i are indicated using the subscript $(\cdot)_i$, while quantities associated with the generic segment j are labeled with the superscript $(\cdot)^j$. In each shooting segment Ω^i , the control vector is discretized as $\mathbf{u}^i(t) = \sum_{j=1}^{N_c^i} s_j(t) \mathbf{u}_j^i$, where $s_j(t)$ are basis functions, in particular cubic splines in the

present implementation, and \mathbf{u}_j^i are N_c^i discrete control vectors. The present implementation allows for a different number of controls DOFs on each segment i , as indicated by the notation N_c^i .

Notice that we confine the control approximations on each shooting segment, instead of considering interpolations across segment boundaries; this has the effect of decreasing the computational cost of finite differencing by increasing the problem sparsity. The code allows for constraints to be enforced at the shooting segment boundaries to enforce the continuity of the controls up to C^1 .

Furthermore, constraints need to be enforced for the state variables between arcs. Since we are dealing with DDEs, these gluing conditions are line constraints covering a time interval of length equal to the delay. For this purpose, in this work we use local expansions to approximate the state variables over the intervals $[t_i - \tau, t_i]$, for reasons which will be made clear in the following. These interpolations can be expressed as follows:

$$\mathbf{y}_i(\xi) \triangleq \mathbf{y}(t_i - \tau\xi) = \sum_{k=1}^K \Phi_k(\xi) \mathbf{a}_{ik}, \quad i = 0, \dots, N_a, \quad \xi \in [0, 1], \quad (74)$$

where $\xi = \eta/\tau$ defines a dimensionless delay, $\mathbf{a}_{ik} \in \mathbb{R}^{n_y}$ are interpolation coefficient vectors, while $\Phi_k(\eta)$, $k = 1, \dots, K$ are the interpolation basis functions.

It is convenient to rewrite the last relations in the following compact vectorial form:

$$\mathbf{y}_i(\xi) = \mathbf{A}_i \mathbf{n}(\xi), \quad i = 0, \dots, N_a, \quad \xi \in [0, 1], \quad (75)$$

where $\mathbf{A}_i \in \mathbb{R}^{n_y \times K}$ is the i th interpolation coefficient matrix defined as

$$\mathbf{A}_i = \left[\mathbf{a}_{i1} \mid \mathbf{a}_{i2} \mid \dots \mid \mathbf{a}_{iK} \right], \quad (76)$$

and $\mathbf{n}(\xi) \in \mathbb{R}^K$ is the vector containing all basis functions:

$$\mathbf{n}(\xi) = (\Phi_1(\xi), \Phi_2(\xi), \dots, \Phi_K(\xi))^T. \quad (77)$$

The optimization variables of the NLP problem stemming from the DMSDDE formulations are represented by the coefficients of the matrices \mathbf{A}_i at each line gluing interface between shooting segments, the control DOFs \mathbf{u}_j^i on each shooting segment, and the final simulation time T for problems with unknown final time, i.e.

$$\mathbf{x} = \left(\mathbf{a}_{(i=0, \dots, N_a; k=1, \dots, K)}^T, \mathbf{u}_{(j=1, \dots, N_c^i)}^{(i=1, \dots, N_a)^T}, T \right)^T, \quad (78)$$

In fact, it should be noted that the coefficients of matrix \mathbf{A}_{i-1} can be used to approximate the initial line data for the integration over the i th arc, with $i = 1, \dots, N_a$. In other words, given matrix \mathbf{A}_{i-1} , the simulation time T and the control parameters \mathbf{u}_j^i , one can integrate numerically the equations of motion over the i th arc, $i = 1, \dots, N_a$, to obtain the states history along each arc.

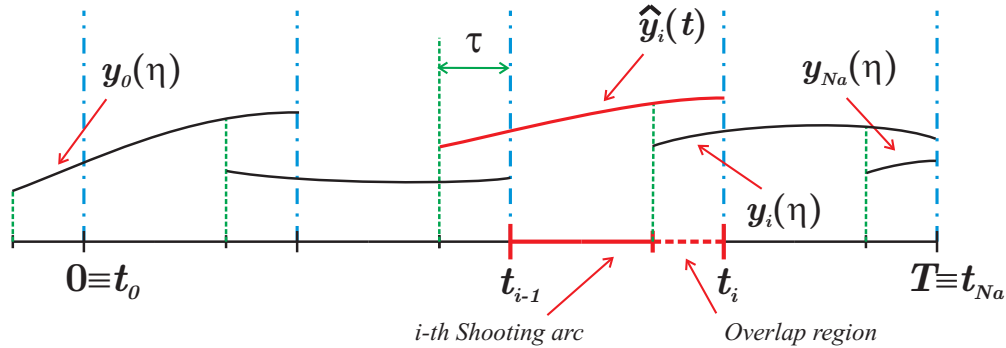


FIG. 12: Line continuity conditions of a single component of the state vector.

Next, the tail of each arc needs to be glued with the head of the next one, in order to enforce the continuity of the states between subsequent integration arcs. In fact, as shown in Fig. 12, the result of the numerical integration over the i th arc $[t_{i-1}, t_i]$, $i = 1, \dots, N_a$, provides knowledge of the current estimate of the state time history along the arc itself; the solution overlaps with the interval $[t_i - \tau, t_i]$, which is the time range related to the initial data of the $i + 1$ arc. Denoting with $\hat{\mathbf{y}}_i(t)$ the simulation results computed by forward integration over the i th arc, the continuity conditions can be expressed as

$$\hat{\mathbf{y}}_i(t_i - \tau\xi) = \mathbf{y}_i(\xi) = \sum_{k=1}^K \Phi_k(\eta) \mathbf{a}_{ik}, \quad i = 1, \dots, N_a, \quad \xi \in [0, 1], \quad (79)$$

Again it is convenient to write the continuity conditions in compact form as follows:

$$\hat{\mathbf{y}}_i(t_i - \tau\xi) = \mathbf{A}_i \mathbf{n}(\xi), \quad i = 1, \dots, N_a, \quad \xi \in [0, 1]. \quad (80)$$

The integration process is based on a numerical discretization scheme, and therefore, in the overlap region $[t_i - \tau, t_i]$, the states are known at discrete times corresponding to the N_i integration mesh points, i.e

$$\hat{\mathbf{y}}_i(t_i - \tau\xi_n), \quad n = 1, \dots, N_i, \quad i = 1, \dots, N_a. \quad (81)$$

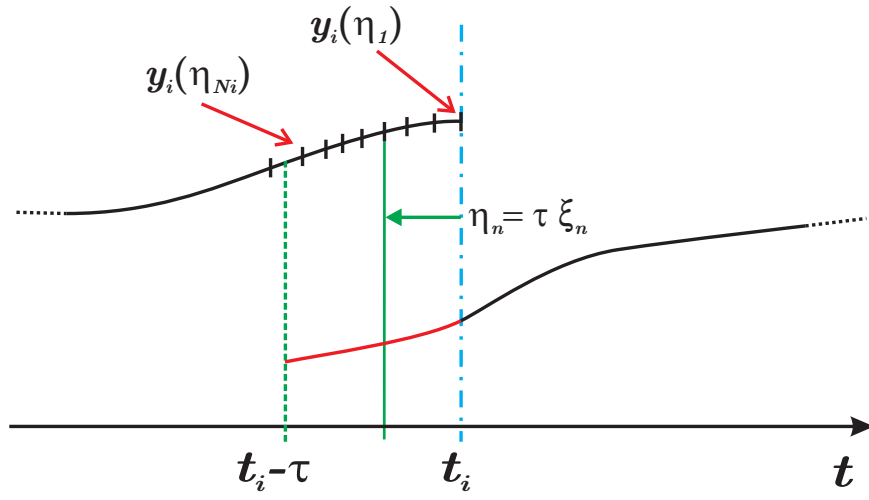


FIG. 13: Overlap region.

Figure 13 shows a detail of the overlap region $[t_i - \tau, t_i]$ and of the corresponding integration points. It should be noted that, in general, N_i may vary with the overlap region i considered, as indicated by the notation, especially if an adaptive integrator is used. If relations (80) are evaluated at the integration mesh points, they become

$$\hat{\mathbf{y}}_i(t_i - \tau \xi_n) = \mathbf{A}_i \mathbf{n}(\xi_n), \quad n = 1, \dots, N_i, \quad i = 1, \dots, N_a. \quad (82)$$

The last set of equations can be rewritten in the following compact form:

$$\hat{\mathbf{Y}}_i = \mathbf{A}_i \mathbf{D}_i, \quad i = 1, \dots, N_a. \quad (83)$$

where the matrix of known coefficients $\hat{\mathbf{Y}}_i \in \mathbb{R}^{n_y \times N_i}$ is defined as

$$\hat{\mathbf{Y}}_i = \left[\hat{\mathbf{y}}_i(t_i - \xi_1) \mid \hat{\mathbf{y}}_i(t_i - \xi_2) \mid \dots \mid \hat{\mathbf{y}}_i(t_i - \xi_{N_i}) \right], \quad (84)$$

while $\mathbf{D}_i \in \mathbb{R}^{K \times N_i}$ is the matrix of basis functions evaluated at the integration points

$$\mathbf{D}_i = \left[\mathbf{n}(\xi_1) \mid \mathbf{n}(\xi_2) \mid \dots \mid \mathbf{n}(\xi_{N_i}) \right]. \quad (85)$$

Transposing Eqs. (83), we obtain

$$\mathbf{D}_i^T \mathbf{A}_i^T = \hat{\mathbf{Y}}_i^T, \quad i = 1, \dots, N_a, \quad (86)$$

which, for a given i , can be considered as a matrix linear system, whose unknowns are the coefficients of matrix \mathbf{A}_i . In other words, the problem corresponds to a set of n_y linear

systems, each having N_i equations and K unknowns. Since typically $N_i \gg K$, the linear system is over-constrained, and it can be readily solved through a least-squares approach. Pre-multiplying Eqs. (86) by \mathbf{D}_i gives

$$\mathbf{D}_i \mathbf{D}_i^T \mathbf{A}_i^T = \mathbf{D}_i \hat{\mathbf{Y}}_i^T, \quad i = 1, \dots, N_a, \quad (87)$$

which enforces state continuity along the overlap region $[t_i - \tau, t_i]$, $i = 1, \dots, N_a$ in a least-squares sense. The matrix system (87) is not explicitly solved in our implementation, but rather it provides a set of constraints to the parametric optimization problem.

Notice that an alternative approach to guaranteeing the continuity of the states at the line gluing segments would consist in imposing equality conditions at each integration point over the overlap region. In this case, the states at the integration nodes along the overlap regions $\mathbf{y}_i(\xi_n)$ would have to be treated as optimization variables, instead of the interpolation coefficients \mathbf{a}_{ik} . The continuity conditions would be simply written as

$$\hat{\mathbf{y}}_i(t_i - \tau \xi_n) = \mathbf{y}_i(\xi_n), \quad n = 1, \dots, N_i, \quad i = 1, \dots, N_a. \quad (88)$$

This approach leads to a simple formulation, which however suffers from two major disadvantages. First, the point equality conditions require $n_y \times N_i$ variables and constraints for each overlap region. In contrast, the least-square approach yields a number of local unknowns and constraints equal to $n_y \times K$. Since typically $N_i \gg K$, the point constraint approach implies a larger dimension of the resulting NLP problem. Second, the least squares method is well suited when an adaptive time step integrator is used, for which the number of integration points N_i in the overlap region is not known a-priori. The dimension of the NLP problem obtained by imposing the point-by-point equality conditions depends instead on the parameters N_i , $i = 1, \dots, N_a$, which would need to be assigned a-priori.

The discretization of the original optimal control problem with the method described in this section results in a non-linear discrete parameter optimization problem, that can be written as

$$\begin{aligned} \min_{\mathbf{x}} K(\mathbf{x}), \\ \text{s.t.: } \phi(\mathbf{x}) \leq 0, \end{aligned} \quad (89)$$

where $K(\mathbf{x})$ is the discrete version of the cost function J of Eq. (66); K is a function of the optimization variables \mathbf{x} defined in Eq. (78), and is evaluated numerically in terms

of the interpolations of the controls and of the time histories of the states obtained by forward time integration within each shooting segment. Furthermore, $\phi(\mathbf{x})$ is a vector function which gathers all problem equality and inequality constraints, including the state continuity conditions at the overlap regions expressed by relations (87), continuity conditions on the controls at the segment boundaries, initial and final conditions, and all constraints and bounds on states and controls. Notice that constraints on the states can only be explicitly enforced in terms of the state optimization unknowns, which however are defined only at the line gluing segments. Segment internal constraints need then be enforced through approximate ad hoc procedures, whose treatment however go beyond the scopes of this work.

NLP problem (89) can be solved efficiently by sequential quadratic programming (SQP) methods [20], as in this work, or interior point (IP) algorithms [21].

IV. NUMERICAL EXAMPLES AND APPLICATIONS

This section describes the application of the proposed methodology to the optimization of representative maneuvers for the notional design of a supercavitating vehicle [3, 6], whose main dimensions and configuration parameters are summarized in Table I. The vehicle controls \mathbf{u} include the throttle δ_s , the cavitator deflection δ_c , the elevator rotation δ_e , and the rotations of the upper and lower fins, denoted respectively as δ_{vu} and δ_{vl} . The formulation is general and can be easily extended to include additional controls which may be added as part of future studies. In particular, the possibility of thrust vectoring and additional actuation degrees of freedom on the cavitator can be considered as viable alternatives to improve the vehicle maneuverability. In fact, the developed trajectory optimization tools may be used as part of a design process in order to estimate the advantages of these possible design modifications.

In this study, the total mass is considered constant throughout the short maneuver here investigated, although further extensions to reflect mass reduction associated with fuel consumption and expulsion of ventilation gases can be considered as part of future refinements. Also, all the maneuvers have been computed assuming a fixed cavitation number, which has been properly selected so as to ensure that the cavity fully envelopes the body at all times. This assumption relies on the hypothesis that the cavity pressure can be adjusted to compensate for variations in the vehicle velocity to maintain the desired value of σ . This

in principle could be achieved through proper cavity ventilation and control of the cavity pressure. In general, however it is still not clear if a refined control on the cavity pressure can in fact be achieved, and which supporting technology might be needed.

The optimization cost function used in the following analyses is defined as

$$J = T^2 + \rho \int_{T_0}^T \dot{\mathbf{u}} \cdot \dot{\mathbf{u}} dt, \quad (90)$$

where T denotes the total unknown time required to perform a desired maneuver, while the second term of the cost includes the control velocities $\dot{\mathbf{u}}$. This second contribution is here introduced to limit the control rates and the tendency of obtaining “bang-bang” type solutions. Also, in Eq. (90), ρ is a user-adjustable weighting parameter used for scaling the contribution of the two terms of the cost.

TABLE I: Model parameters.

Model parameters		
<i>Name</i>	<i>Symbol</i>	<i>Value</i>
mass	M	150 Kg
roll moment of inertia	A	0.75 Kg m ²
pitch/yaw moment of inertia	B	200 Kg m ²
vehicle length	L	4 m
vehicle diameter	D	0.2 m
center of gravity abscissa measured form the cavitator	x_{cg}	2 m
cavitator diameter	d_c	0.07 m
fin abscissæ measured from the cavitator	x_F	3.5 m
fin length	l_F	0.25 m
maximum thrust	T_{\max}	33e3 N
Hydrodynamic parameters		
<i>Name</i>	<i>Symbol</i>	<i>Value</i>
cavitation number	σ	0.02
cavitator drag coefficient	C_{D0}	0.805
water density	ρ_l	1000 Kg/m ³
water kinematic viscosity	ν_l	1.14e-6 m ² /s

A. Dive Maneuver

We study initially a simple two-dimensional dive maneuver, with the objective of comparing the solutions with those obtained from the application of the DT technique on the ODE model of Ref. [7]. We consider the vehicle initially flying at a trimmed straight and level flight condition at 85 m/s, and we wish to find an optimal trajectory that involves diving to an assigned depth of 20 m; at the end of the depth change maneuver, the vehicle returns to a trimmed flight condition at the same initial speed.

The trajectory computed with the present DMSDDE technique is shown in Fig. 14, where it is compared with the one obtained by DT [7]. Specifically, the dotted line refers to the DDE model and was computed by using one single shooting arc, the control history being described by 20 equally spaced control DOFs. It should also be noted that there is just a single set of least square constraints (87) in this case, which are used to enforce the final trim conditions. The dash-dotted line refers to the ODE model computed using the DT method, with the simulation domain discretized into 80 steps. The number of time steps was selected on the basis of a convergence study of the solution by means of a grid refinement technique. For the DMSDDE simulation, a similar approach was used to choose an appropriate number of control DOFs and the time step size for the time marching within the shooting segments. Thus, since both solutions appear to be at convergence, any differences between the two approaches can be interpreted as due to differences between the two models, rather than to discrepancies between the MS and DT solutions.

The two trajectories in Fig. 14 appear to be quite different, in particular in terms of the horizontal displacement required for the DDE model to achieve the assigned depth. Significant differences can be also observed from the variation of the pitch angle versus time presented in Fig. 15, which shows how the maneuvering time evaluated using the DDE model is significantly longer, and how the maximum pitch (in absolute value) of the vehicle remains lower.

The pitch angle estimated using both models reaches its final value with a zero rate, as required for the arriving state to be at trim. This behavior is however more pronounced in the DDE case, as a result of the time delay in the system imposing the requirement of a line condition, rather than a point one as in the ODE case. Physically, this translates the need for the vehicle to remain around the trim pitch value for a time sufficient for the cavity to

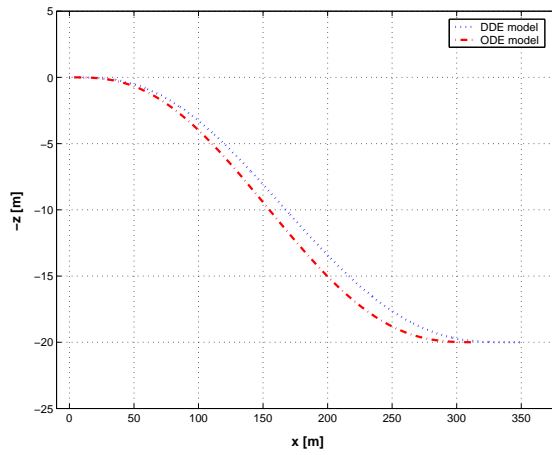


FIG. 14: Dive trajectories for the ODE and DDE models.

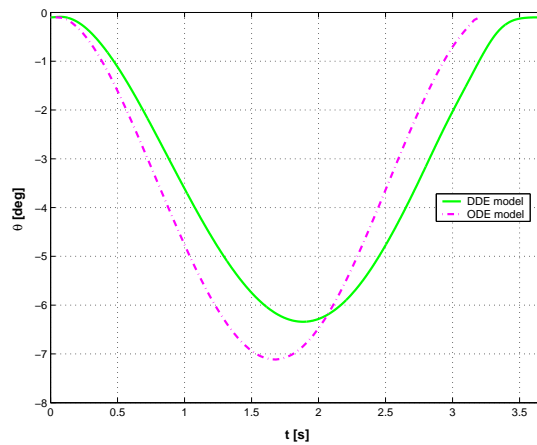


FIG. 15: Pitch angle variation during the minimum time dive maneuvers for the ODE and DDE models.

remain horizontal and steady with respect to the vehicle.

A similar observation can be made from the analysis of the time histories of the controls presented in Fig. 16. The solid lines refer to the DMSDDE simulation, and the star symbols indicate the cubic spline control DOFS. On the other hand the dash-dotted lines are associated with the DT solution, and the discrete control parameters are indicated using circles. Both cavitator and elevator angles reach their steady/trim state with zero rate, to suggest again the need to achieve a steady configuration of the cavity and of the hydrodynamic forces at the end of the maneuver. The value of the throttle, in contrast, does not affect the hydrodynamic interactions of the vehicle, as it only corresponds to an axial thrust force,

which, within the modeling assumptions, is not coupled in any way with the behavior of the cavity.

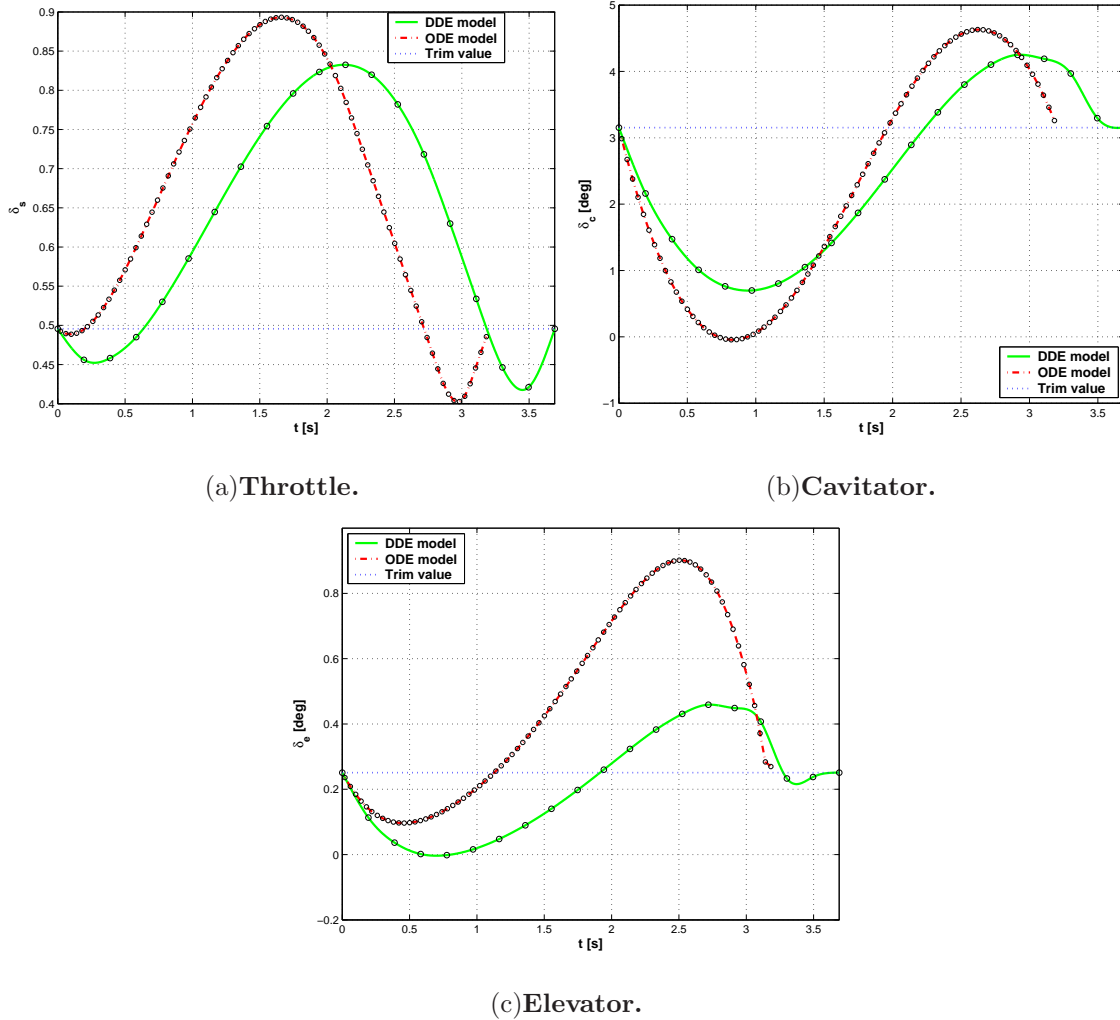
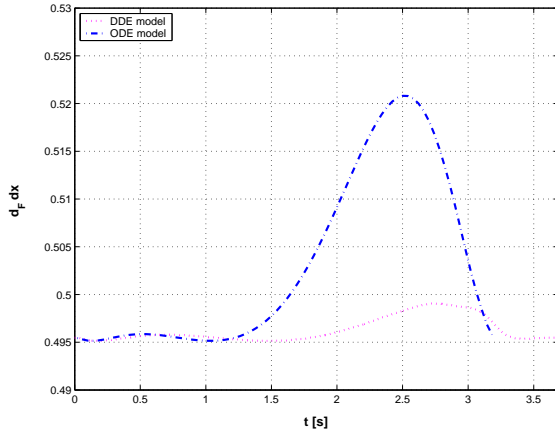
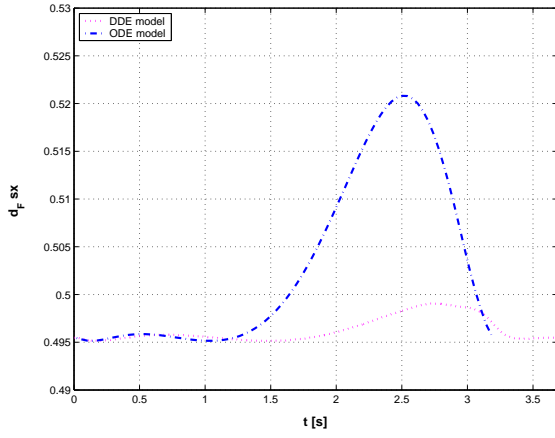


FIG. 16: Control time histories for the minimum time dive for the ODE and DDE models.

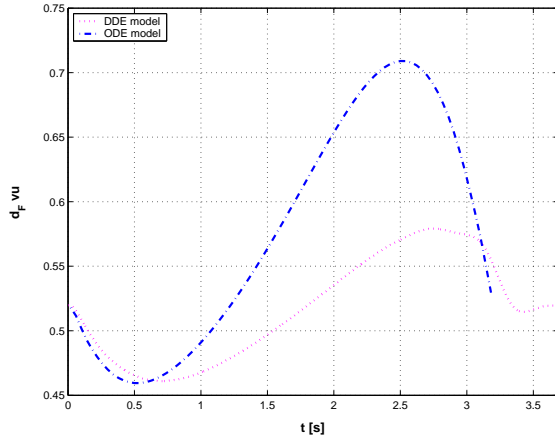
The differences between solutions and associated cavity models can be finally analyzed through the time histories of the fin immersion depths, shown in Fig. 17. The important discrepancies in fin immersion can be attributed to the different cavity shapes: if on the one hand the radius distribution is the same, according to Logvinovich’s formula 16, on the other hand the cavity axes have different definitions as discussed in IIC. As illustrated in Fig. 17, the delayed cavity model is more centered at the fin section resulting in smaller variations of fin immersions. The steady state conditions achieved by the cavity at the end of the maneuver are again highlighted by the rate of the immersion ratios approaching zero upon completion of the dive.



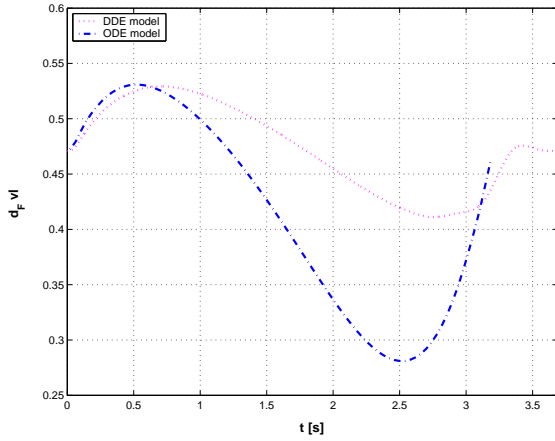
(a) Right horizontal fin.



(b) Left horizontal fin.



(c) Upper vertical fin.



(d) Lower vertical fin.

FIG. 17: Fin relative immersions for the minimum time dive for the ODE and DDE models.

It is finally important to note that both maneuvers were obtained for the same weighting factor $\rho = 1/10$. This particular value strongly favors the maneuvering time with respect to the control rates, and this automatically implies more aggressive maneuvers. This weight selection highlights the differences between the two models, while higher values of ρ , corresponding to longer and less aggressive maneuvers, would yield increasingly similar maneuvers.

B. Family of Turns

The second type of maneuvers considered in the present study requires the vehicle to perform a turn corresponding to an assigned change in the heading angle. These maneuvers are more complex than the previous ones, as they involve variations of all 6 degrees of freedom of the vehicle. Specifically, the vehicle, initially at trim flying with an horizontal velocity of 85 m/s, is required to achieve the same trim setting after the specified change in heading. Solutions are found for minimum time turns with assigned final heading angle ranging from 10 to 90 degrees. The boundary conditions further specify that initial and final depths should be the same.

Optimal trajectories found with the DMSDDE approach are shown in Fig. 18. The results for increasing required heading change are obtained using a continuation technique, whereby the solution for a given angle is used as a starting guess for the subsequent maneuver. The first turn corresponding to a 10 degree change is calculated using as a starting guess the steady state and the control values corresponding to the initial trim condition. Each solution is characterized by a single shooting arc and 20 equally spaced DOFs for the single control input.

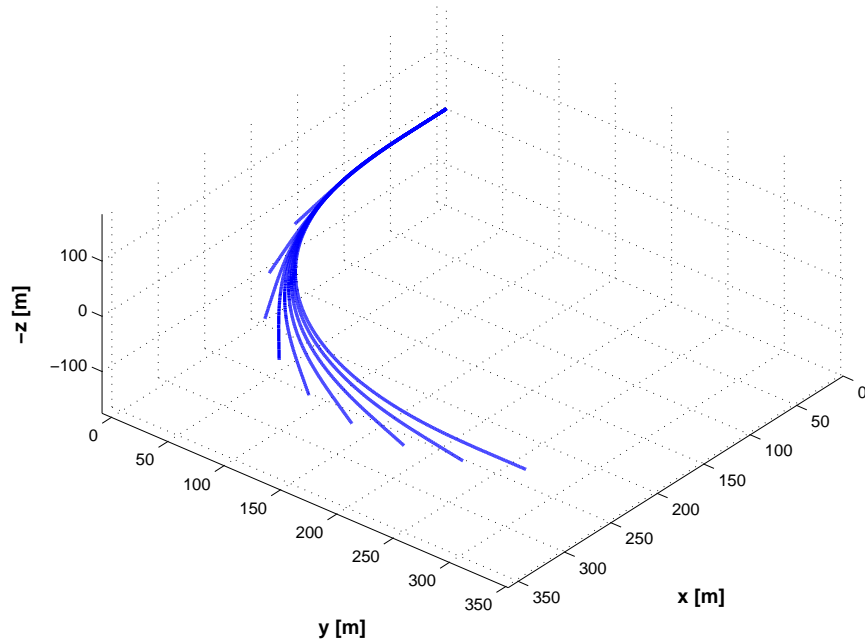
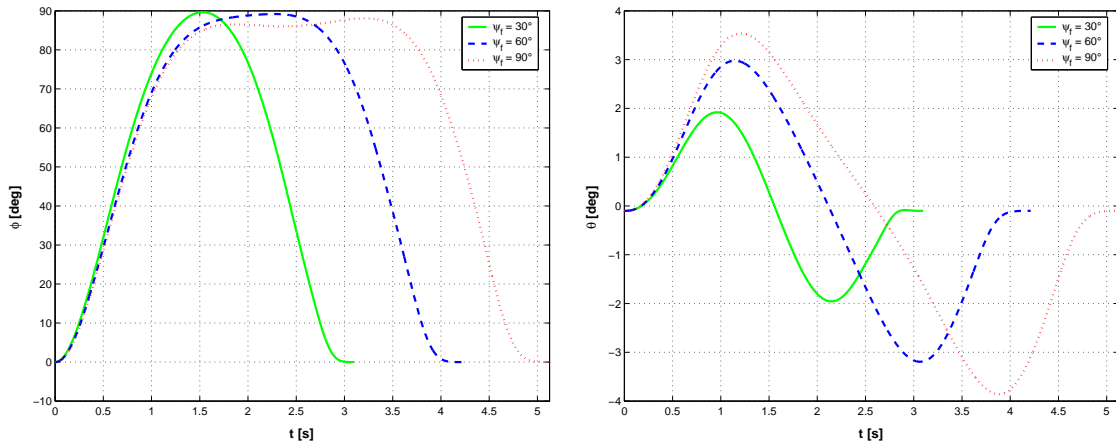


FIG. 18: Family of turns.

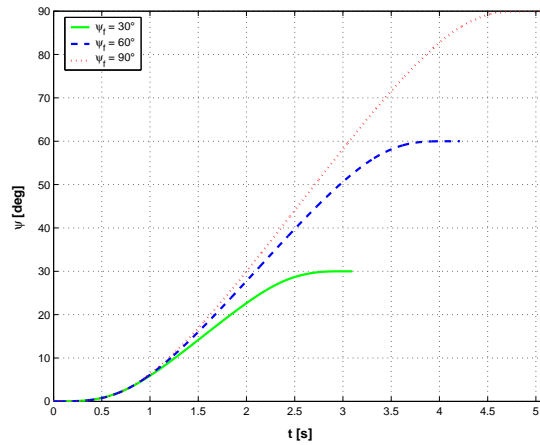
Figure 19 shows the variations of the vehicle Euler angles (in the 3-2-1 sequence), com-

puted from the quaternions used for the parametrization of rotations in the formulation, for some representative turns. The results show that the vehicle undergoes significant roll and pitch during the maneuvers, which show how all the trajectories can be classified as fully three dimensional. In particular, Fig. 19(a) show that all maneuvers imply maximum rolls close to 90 degrees. This very pronounced roll is in fact needed for the 1 degree of freedom cavitator to generate sufficient lift to counterbalance the centripetal force during turning. A more sophisticated vehicle, with additional controllable degrees of freedom, may be considered in order to reduce or eliminate the need for such a pronounced roll. The variation of the pitch angle presented in Fig. 19(b) confirms the three-dimensional nature of the turn maneuvers.



(a) Roll angle.

(b) Pitch angle.



(c) Heading angle.

FIG. 19: Euler angles for representative minimum time turns.

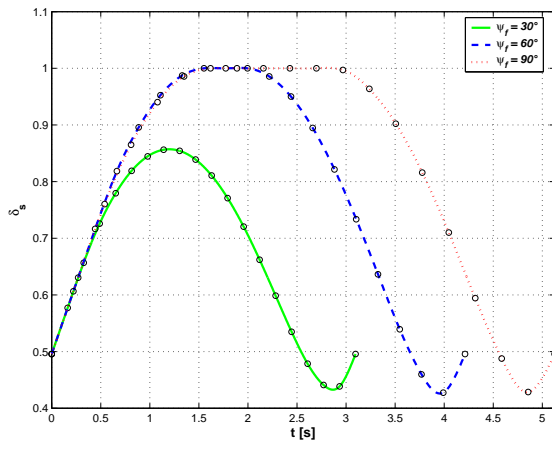
Finally, the variations from trim of the control inputs are presented in Fig. 20: each input is different from zero and at the boundaries of the domain is equal to the corresponding trim value associated to the flight velocity of 85 m/s. As in the previous case, all of the controls, with the exception of the throttle, tend to gradually return to the trim values with an approximately zero rate condition.

It is important to note that in all maneuvers considered in this and previous sections the vehicle does not come in contact with the cavity. The absence of vehicle/cavity contacts was not specifically enforced through constraints, and can be attributed to the fact that impact phenomena imply an increase in drag as well as an increase in the control rates in response to the contact itself. Both effects correspond to an unfavorable increase of the considered cost function (90) defining the maneuver requirements. In general, however, and particularly for highly aggressive maneuvers, the absence of contacts with the cavity can be imposed as part of the definition of the maneuver itself, with the objective to avoid, or minimize the occurrence of drag increase, high control rates, vibrations, noise, etc.

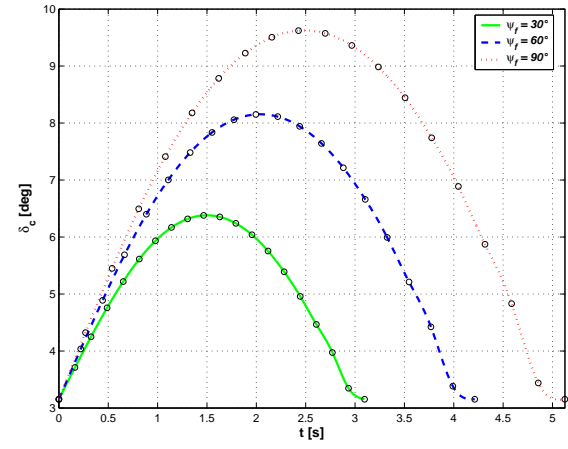
V. CONCLUSIONS

This paper has presented a flight mechanics model for supercavitating vehicles governed by DDEs. Time delays were introduced by memory effects related to the cavity formation process. In addition, optimal maneuvers were formulated as appropriate optimal control problems.

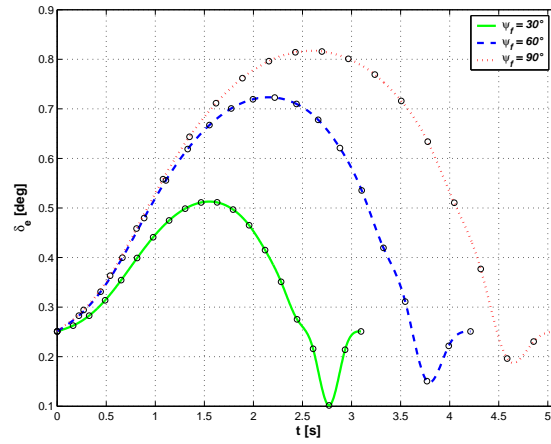
The solution of optimal control problems for DDE-governed systems of the complexity of the present flight mechanics model are extremely challenging multi-point boundary value problems, for which general and robust algorithms were not previously available in the literature. In the present work we have proposed a new direct approach based on the multiple shooting technique, termed here DMSDDE. The direct nature of the approach means that one does not need to derive the optimal control governing equations, a daunting task for complex models, and even more so for DDE-governed systems. Furthermore, the multiple shooting solution allows for the use of potentially very small time step sizes for resolving the fast dynamics temporal scales of the solution, without affecting the discrete optimization problem size. Finally, the gluing line conditions were treated in an efficient manner by using local approximations of the states based on spline interpolations; this enables time-step-size-



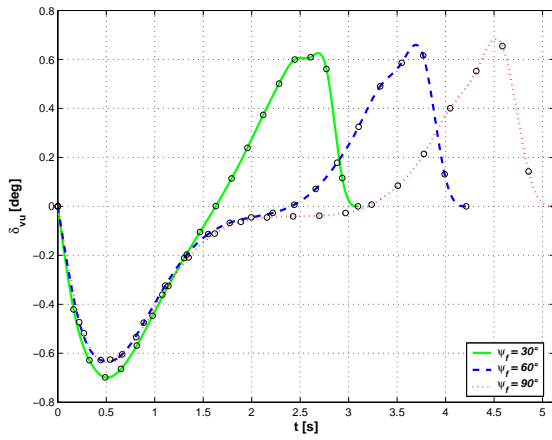
(a) Throttle.



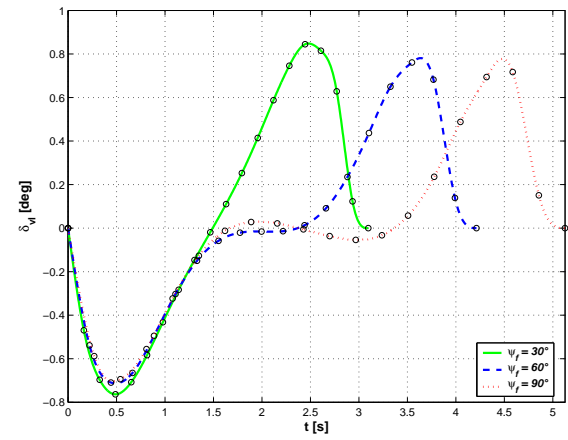
(b) Cavitor.



(c) Elevator.



(d) Upper rudder.



(e) Lower rudder.

FIG. 20: Controls for representative minimum time turns.

adaptive time marching and drastically reduces the number of problem unknowns.

The formulation has been tested on some preliminary but representative examples, involving dives and turns. The presented results show that for aggressive maneuvers it is very important to take into account the memory effects of the gaseous cavity when computing an optimal trajectory, and therefore apply the proposed DMSDDE technique.

The general trajectory optimization framework is formulated in a way that enables its application to a variety of other more complex scenarios. For example, the configuration of the vehicle can be parameterized in terms of a set of design variables which can be then optimized under specific requirements dictated by maneuverability constraints, as first described in Ref. [8]. Such constraints could be formulated to reduce or eliminate cavity-body interactions and vibrations during maneuvering flight, with obvious advantages. Future research should also extend the present studies to carry out comparisons of the behavior of maneuver tracking controllers. In fact, it is fully expected that trajectories obtained through the proposed optimization framework, being compatible with the vehicle dynamic equations which appear explicitly as constraints of the optimization problem, are more easily trackable than trajectories obtained as interpolations of way points or other ad-hoc procedures.

-
- [1] D. Miller, *Going to war in a bubble*, International Defense Review (1995).
 - [2] I. N. Kirschner, N. E. Fine, J. James S. Uhlman, and D. C. Kring, RTO AVT lecture series on supercavitating flows, Von Karman Institute, Brussels Belgium (2001).
 - [3] I. N. Kirschner, D. C. Kring, A. W. Stokes, N. E. Fine, and J. James S. Uhlman, *Journal of Vibration and Control* **8**, 219 (2002).
 - [4] J. Dzielski and A. Kurdila, *Journal of Vibration and Control* **9**, 791 (2003).
 - [5] E. H. Abed, B. Balachandran, and G. Lin, *Control of supercavitating bodies and bodies with partial cavity*, The Institute for Systems Research, University of Maryland College Park, presentation material at ONR Meeting (2005).
 - [6] M. Ruzzene and F. Soranna, *Journal of Vibration and Control* **10**, 243 (2004).
 - [7] M. Ruzzene, R. Kamada, C. L. Bottasso, and F. Scorcelletti, *Journal of Vibration and Control* (2007), to appear.
 - [8] S. S. Ahn, M. Ruzzene, C. Bottasso, and F. Scorcelletti, *IEEE Journal of Oceanic Engineering*

- (2007), under review.
- [9] M. Borri, L. Trainelli, and C. Bottasso, *Multibody System Dynamics* **4**, 129 (2000).
 - [10] G. V. Logvinovich, Tech. Rep., U.S. Department of Commerce, Washington, DC (1972), translated from the Russian(NASA-TT-F-658).
 - [11] T. Kiceniuk, CIT Hydrodynamic Report E-12.17, California Institute of Technology, Pasadena, CA (1954).
 - [12] A. May, SEAHAC Technical Report 75-2, Naval Surface Weapons Center, White Oak Laboratory, Silver Spring, MD (1975).
 - [13] N. E. Fine and S. A. Kinnas, *Journal of Ship Research* **37** (1993).
 - [14] S. E. Hassan (2004), private communication.
 - [15] G. V. Logvinovich, Trudy TsAGI 2052, Central Aero and Hydordyanmics Institute, Moscow, Russia (1980), translated from Nekotoryyi voprosy glissirovaniya ikavitatsii [Some problems in planing and cavitation].
 - [16] F. M. White, *Fluid Mechanics* (McGraw-Hill, New York, 1994), 3rd ed.
 - [17] J. Arthur E. Bryson and Y.-C. Ho, *Applied Optimal Control* (Hemisphere Publishing Corporation, New York, 1975).
 - [18] J. T. Betts, SIAM (2001).
 - [19] F. Scorcelletti, C. L. Bottasso, and M. Ruzzene, In preparation (2007).
 - [20] A. Barclay, P. E. Gill, and J. B. Rosen, Report NA 97-3, Department of Mathematics, University of California, San Diego, CA (1997).
 - [21] J. Renegar, SIAM, Philadelphia (2001).